RESEARCH



Stress-constrained optimization of multiscale structures with parameterized microarchitectures using machine learning

Nolan Black¹ · Ahmad Najafi¹

Received: 21 November 2023 / Revised: 9 May 2024 / Accepted: 18 May 2024 © The Author(s) 2024

Abstract

A multiscale topology optimization framework for stress-constrained design is presented. Spatially varying microstructures are distributed in the macroscale where their material properties are estimated using a neural network surrogate model for homogenized constitutive relations. Meanwhile, the local stress state of each microstructure is evaluated with another neural network trained to emulate second-order homogenization. This combination of two surrogate models — one for effective properties, one for local stress evaluation — is shown to accurately and efficiently predict relevant stress values in structures with spatially varying microstructures. An augmented lagrangian approach to stress-constrained optimization is then implemented to minimize the volume of multiscale structures subjected to stress constraints in each microstructure. Several examples show that the approach can produce designs with varied microarchitectures that respect local stress constraints. As expected, the distributed microstructures cannot surpass density-based topology optimization designs in canonical volume minimization problems. Despite this, the stress-constrained design of hierarchical structures remains an important component in the development of multiphysics and multifunctional design. This work presents an effective approach to multiscale optimization where a machine learning approach to local analysis has increased the information exchange between microand macroscales.

 $\textbf{Keywords} \ \ \text{Topology optimization} \cdot \text{Multiscale design} \cdot \text{Stress-constrained design} \cdot \text{Machine learning} \cdot \text{Second-order homogenization}$

1 Introduction

The design of multiscale structures aims to strategically distribute material with tailored properties. Inspired by natural structures like bamboo and trabecular bone (Wegst et al 2015), multiscale design optimization can harness the exotic behavior of optimized cellular materials (Surjadi et al 2019) to achieve superior multi-functional performance at the observable scale (Wu et al 2021a). In particular, multiscale structures with spatially varying microarchitectures have been shown to exhibit exceptional performance in energy-absorbing, buckling, and post-yield applications (Alberdi et al 2020; Wang and Sigmund 2020; Kochmann

Responsible editor: Marco Montemurro

Ahmad Najafi arn55@drexel.edu

Published online: 08 June 2024

and Bertoldi 2017). The relationship between the macroscale (observable space) and microscale (material space), however, leads to a complicated exchange of physical effects that increases the computational burden of design optimization. A successful optimization framework must exchange the appropriate physical information between scales, navigate a multiscale design space, and limit the computational cost of iterative optimization.

Several approaches to multiscale structural optimization have emerged since the seminal work of Bendsøe and Kikuchi (1988). Approaches differ in their treatment of the scale separation between the macroscale structure and local changes in microstructure, but the homogenization approach is ubiquitous in multiscale design (Wu et al 2021a). As it is employed in design optimization approaches, the homogenization model of multiscale materials considers variations of the microstructure that are sufficiently small relative to the macroscale structure (Guedes and Kikuchi 1990; Allaire 2012; Najafi et al 2021). Homogenization produces



Department of Mechanical Engineering and Mechanics, Drexel University, Philadelphia, PA 19104, USA

the effective or homogenized properties of a microstructure design through analysis of a unit-cell boundary value problem.

Homogenization-driven design optimization links the effective properties of a unit-cell design to a set of design variables to evaluate the performance of a structure with evolving topologies. For example, optimization frameworks have considered the design of microscale topologies and the layout of the homogenized macroscale structure, resulting in a series of nested optimization problems (Nakshatrala et al 2013; Xia and Breitkopf 2014). The additional computational cost and potential geometric incongruities in the nested approach to homogenization-based optimization motivates a reduced, parameterized representation of microarchitecture. Truss-like microarchitectures, parameterized by geometric descriptors, provide an efficient representation of the microarchitectures (Wang et al 2018; Groen and Sigmund 2017; Wu et al 2021b). Other approaches rely on a database of microarchitectures to efficiently model multiscale structures (Wang et al 2020; Djourachkovitch et al 2021). In a reduced design space, surrogate models can map the design variables to the microarchitecture's effective stiffness, relegating the microscale analysis to more efficient models (White et al 2018; Black and Najafi 2023). Furthermore, post-processing techniques such as the de-homogenization method can be used to recover viable structures from the parameterized microarchitecture descriptors (Pantz and Trabelsi 2008; Groen et al 2021).

In addition to the effective material properties of a unit-cell design, homogenization can provide the effective stresses of the microstructure. These effective macroscale stresses are linked to the true microscale stress state through corrector terms that describe the local stress of composite materials (Allaire 2002). In relation to the local stress within a microarchitecture, the corrector represents a stress amplification at the local scale. Recently the stress amplification tensor has been studied as a metric for the design of architected structures (Ferrer et al 2021; Zhang et al 2022). The incorporation of local stress amplification in multiscale structural optimization motivates a microstructure-aware design framework and will be the focus of this work.

Stress-driven topology optimization incorporates the structure's state of stress as a performance metric. Stress minimization approaches seek the topological layout that minimizes the maximum stress under certain loading conditions (Lian et al 2017), while stress-constrained approaches apply a point-wise stress limit to the structure (da Silva et al 2021a). Several mechanical and computational challenges drive the development of stress-driven design optimization. The singularity phenomenon arises as the material design density approaches zero and the local stress is amplified (Duysinx and Sigmund 1998; Le et al 2010). The optimization, therefore, is unable to remove material (i.e., create

holes) due to the stress amplification. The ϵ -relaxation technique has been widely adopted to resolve the singularity phenomenon by relaxing the stress constraint in areas of low density (Cheng and Guo 1997). Evaluating the stress state at each material point also creates a highly nonlinear, computationally expensive optimization formulation. To incorporate the point-wise stress in the optimization formulation, global stress aggregation has been used to efficiently quantify the structure's stress performance (Duysinx and Sigmund 1998; Luo et al 2013). Point-wise constraints, implemented through the augmented lagrangian approach (Ito and Kunisch 1990), have been also implemented to evaluate stress-constraints locally (Pereira et al 2004; Senhora et al 2020). The augmented lagrangian approach to point-wise stress constraints, along with proper use of stress interpolation parameters, has been shown to be extensible to large-scale stress-constrained structural optimization problems (da Silva et al 2021b).

Stress-driven multiscale design builds upon topology optimization frameworks to incorporate stress metrics across the material (microscale) and structural (macroscale) design domains. The majority of work in this field has so far focused on the stress-driven design of materials where the local microarchitecture is optimized under some stress constraints (Coelho et al 2019; Picelli et al 2020; Collet et al 2018; Alacoque et al 2021; Conde et al 2022). The work of Coelho et al (2021) compares both shape and topology optimization approaches for stress-driven design of microstructures. Interestingly, in this work it is shown that a multimaterial microstructural model can significantly reduce the peak stresses in porous composites.

To incorporate the local microarchitectures into the greater structure, the homogenization correctors may be evaluated to calculate local stress amplification (Allaire et al 2004; Ferrer et al 2021). Correctors are not always known (Allaire 2002), so other approaches estimate a stress amplification factor in the microstructure numerically. For example, isotropic yield models may be estimated as a function of the microarchitecture's relative density (Cheng et al 2019; Zhang et al 2020; Zhao et al 2022). Concurrent optimization has also been used to incorporate the stress state of an evolving microstructure with limited macroscale variance (Zhao et al 2021b, a; Ho-Nguyen-Tan and Kim 2023). These techniques resolve the microstructure's stress state to its maximum value (or an approximation of its maximum).

This paper introduces a microstructural yield criteria in a computational design model for spatially varying microarchitectures. We implement this yield criteria as a local stress constraint, then we evaluate the multiscale phenomena using a machine learning model trained using second-order homogenization. The resulting approach yields an interpolation of the maximum stress within each microstructure as a function of its geometry and macroscale stress state.



The multiscale formulation for stress amplification (including second-order homogenization details) is introduced in Sect. 2, then Sect. 3 introduces the neural network surrogate approach for local stress evaluation. The optimization formulation is presented in Sect. 4. Numerous examples are presented in Sect. 5 to evaluate the design framework. The optimization framework is shown to effectively and efficiently incorporate multiscale effects in the design model, enriching the information exchange between scales through the neural network surrogate models.

2 Multiscale stress amplification

The multiscale system in this work considers a hierarchical structure (Fig. 1a) represented by macroscale domain composed of many small microscale domains (microarchitectures) (Fig. 1b). We seek a model for the amplification of stress at the macroscale caused by local changes in the microscale. In the macroscale, boundary conditions are defined and the material layout is prescribed (Fig. 1b, c). In the microscale, the structural response of each microarchitecture is evaluated through numerical homogenization techniques (Fig. 1d). The multiscale analysis procedure is designed to efficiently estimate local stress-based yield criteria within a structure composed of many spatially varying microarchitectures (Fig. 1e).

The multiscale model presented in this work assumes loosely coupled macroscale-microscale response. This loose coupling is defined by a first-order (Cauchy) macroscale stress-strain relationship and a second-order microscale response (Fig. 2). The following subsections detail this coupling and evaluate the multiscale model compared to direct numerical simulation (fullscale analysis).

2.1 First-order macroscale response

In the macroscale, numerical homogenization is first applied to estimate the effective linear, first-order constitutive relation of each microstructure (Guedes and Kikuchi 1990; Hassani and Hinton 1998). From the relation $\sigma_{ij} = C_{ijkl} \varepsilon_{kl}$ of stress σ_{ii} and strain ε_{kl} , a periodic composite with sufficient

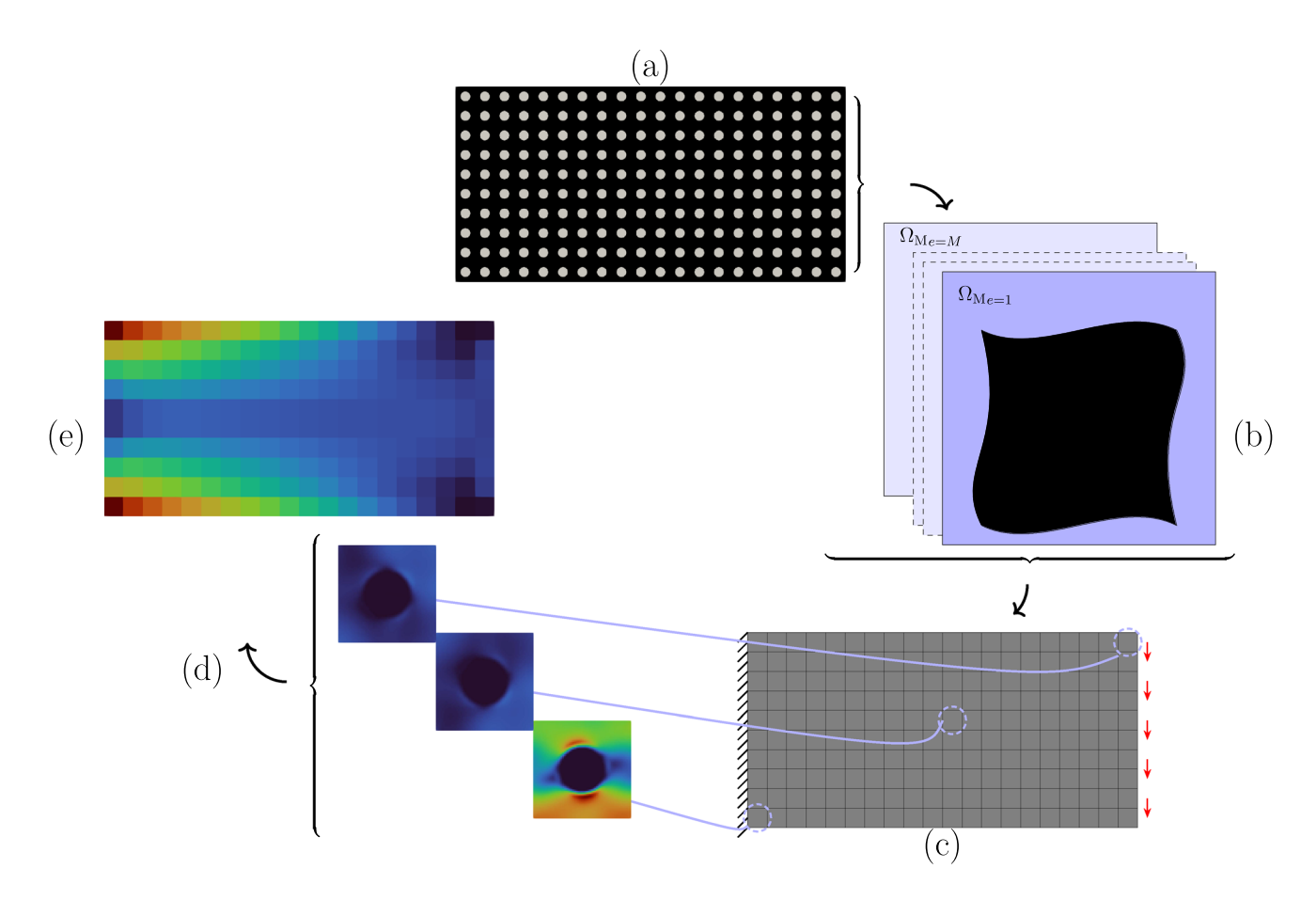


Fig. 1 The procedure for calculation of the stress amplification caused by the presence of microarchitecture is presented. The structure with realized microstructures (a) is homogenized (b) to produce

an approximate macroscale system (c). Based on the macroscale response, a series of local analyses (d) produces the amplified stress in each microstructure (e)



102 Page 4 of 23 N. Black, A. Najafi

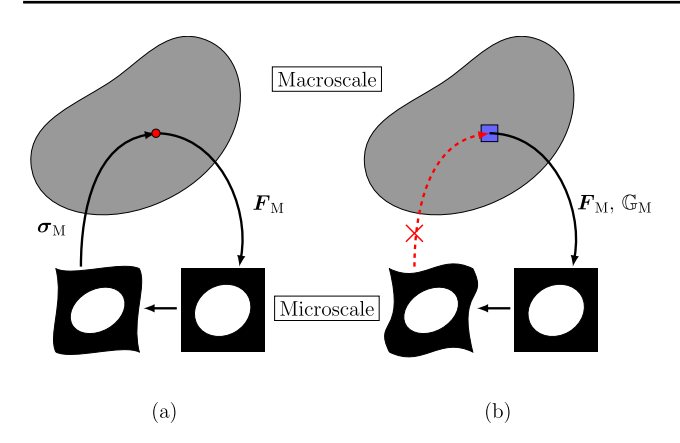


Fig. 2 The multiscale strategy is presented where the macroscale response is approximated using first-order homogenization techniques (a), then a local evaluation with approximate second-order behavior (b) is used to evaluate local stresses. The strategy is *uncoupled* because the higher-order stresses induced in (b) are neglected in the macroscale

separation of length scales (i.e., the characteristic length of the microstructure is significantly smaller than the characteristic length of the structure) may be distilled into the effective constitutive tensor; its definition follows from the Method of Multiscale Virtual Power (De Souza Neto et al 2015; Blanco et al 2016b). We limit this discussion to the case of microscale periodic boundary conditions, infinitesimal strains, and linear elastic material behavior.

First, the process *kinematic insertion* defines the kinematic transition from a macroscale position $x \in \Omega_{\rm M}$ to a microscale position $y \in \Omega_{\mu}$. Without loss of generality, we define the microscale origin at the microstructure's centroid:

$$\int_{\Omega_u} \mathbf{y} dV = \mathbf{0}.\tag{1}$$

The first-order expression for microscale displacement u_{μ} is

$$\boldsymbol{u}_{\mu}(\mathbf{y}) = \boldsymbol{u}_{\mathrm{M}}(\mathbf{x}) + \nabla_{\mathbf{x}} \boldsymbol{u}_{\mathrm{M}}(\mathbf{x}) \cdot \mathbf{y} + \tilde{\boldsymbol{u}}_{\mu}(\mathbf{y}), \tag{2}$$

SC

$$\nabla_{\mathbf{v}} \mathbf{u}_{\mu}(\mathbf{y}) = \nabla_{\mathbf{x}} \mathbf{u}_{\mathbf{M}}(\mathbf{x}) + \nabla_{\mathbf{v}} \tilde{\mathbf{u}}_{\mu}(\mathbf{y}) \tag{3}$$

for the microscale displacement \boldsymbol{u}_{μ} defined for $\boldsymbol{y} \in \Omega_{\mu}$, macroscale displacement $\boldsymbol{u}_{\mathrm{M}}$ defined for $\boldsymbol{x} \in \Omega_{\mathrm{M}}$, and microscale displacement fluctuation $\tilde{\boldsymbol{u}}_{\mu}$. Here we introduce the notation $(\cdot)_{\mathrm{M}}$ to indicate a macroscale quantity and $(\cdot)_{\mu}$ to indicate a microscale quantity (Fig. 3). In defining this space of microstructural deformations, the following averaging relations are postulated:

$$\boldsymbol{u}_{\mathrm{M}} = \frac{1}{|\Omega_{\mu}|} \int_{\Omega_{\mu}} \boldsymbol{u}_{\mu} dV \tag{4}$$

and

$$F_{\rm M} = \frac{1}{|\Omega_{\mu}|} \int_{\Omega_{\mu}} F_{\mu} dV \tag{5}$$

for the deformation gradient $F = I + \nabla u$. The kinematical averaging relations (4) and (5) naturally lead to the following constraints on \tilde{u}_u :

$$\frac{1}{|\Omega_{\mu}|} \int_{\Omega_{\mu}} \tilde{\boldsymbol{u}}_{\mu} dV = \mathbf{0} \tag{6}$$

and

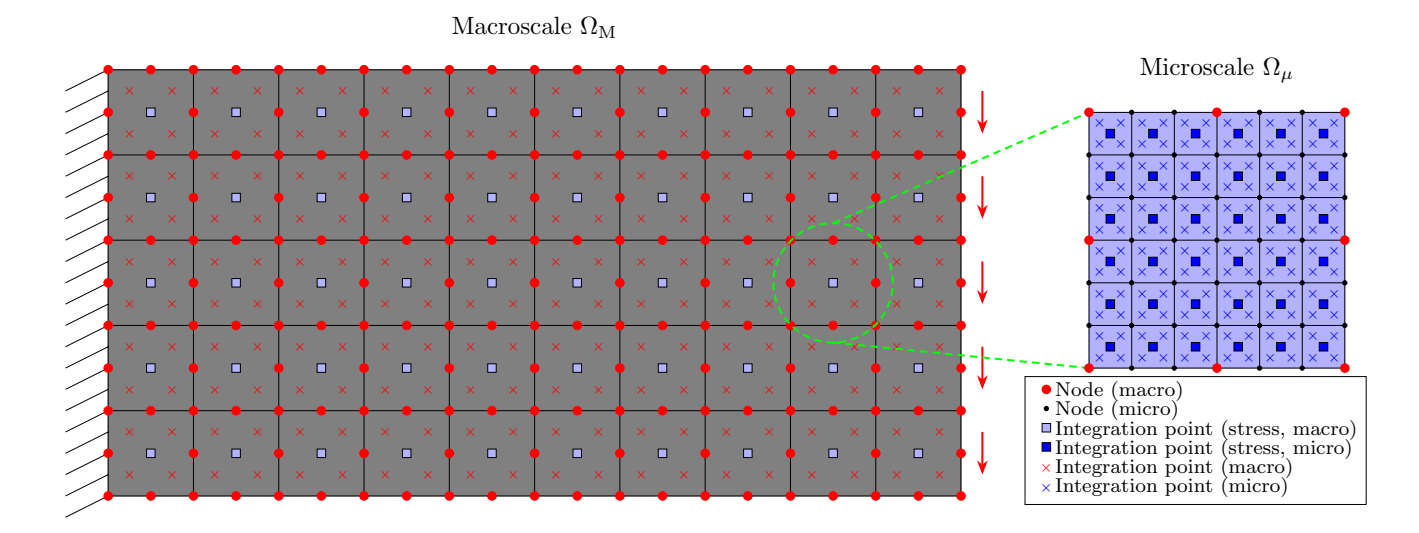


Fig. 3 The multiscale framework in this work considers a discretized macroscale domain $\Omega_{\rm M}$ composed of many microscale domains Ω_{μ} in which the spatially varying microarchitectures are defined



$$\frac{1}{|\Omega_{\mu}|} \int_{\Omega_{\mu}} \nabla_{\mathbf{y}} \tilde{\mathbf{u}}_{\mu}(\mathbf{y}) dV = \mathbf{0}. \tag{7}$$

The constraints (6) and (7) define the minimum viable space of admissible \tilde{u}_{μ} . Periodic boundary conditions are imposed to further restrict this space; although periodicity restricts the microstructural design space to periodic geometries, periodic boundary conditions have been shown to offer a more appropriate approximation of macroscale stresses (Miehe and Koch 2002) which is desirable for this application. We consider a generic set of opposing boundaries Γ^- and Γ^+ with mirrored discretizations. Periodicity is defined by

$$\tilde{\boldsymbol{u}}_{\mu}(\mathbf{y}^{-}) = \tilde{\boldsymbol{u}}_{\mu}(\mathbf{y}^{+}) \tag{8}$$

which ensures constraints (6) and (7) are satisfied (De Souza Neto et al 2015). In conclusion, the space of admissible first-order fluctuations is defined

$$\tilde{\mathcal{V}}_{\mu}^{(1)} = \left\{ \tilde{\boldsymbol{u}}_{\mu} \in \boldsymbol{H}^{1}, \tilde{\boldsymbol{u}}_{\mu}(\mathbf{y}^{-}) = \tilde{\boldsymbol{u}}_{\mu}(\mathbf{y}^{+}) \right\}. \tag{9}$$

The microscale equilibrium condition, expressed as a variational form of the Hill-Mandel condition, ensures equilibrium between scales:

$$\mathbf{P}_{\mathrm{M}} : \delta \mathbf{F}_{\mathrm{M}} = \frac{1}{|\Omega_{\mu}|} \int_{\Omega_{\mu}} \mathbf{P}_{\mu} : \delta \mathbf{F}_{\mu} dV
= \frac{1}{|\Omega_{\mu}|} \int_{\Omega_{\mu}} \mathbf{P}_{\mu} : \left[\delta \mathbf{F}_{\mathrm{M}} + \nabla_{y} \delta \tilde{\mathbf{u}}_{\mu} \right] dV, \tag{10}$$

$$\forall \tilde{\mathbf{u}}_{\mu} \in \tilde{\mathcal{V}}_{\mu}^{(1)}$$

for the macroscale first Piola-Kirchhoff stress tensor $P_{\rm M}$. By considering $\delta F_{\rm M}=0$ and our assumption of small-strain elasticity, the microscale equilibrium condition follows from (10) as

$$0 = \int_{\Omega_{\mu}} \boldsymbol{\sigma}_{\mu} : \nabla_{\mathbf{y}} \delta \tilde{\boldsymbol{u}}_{\mu} dV \quad \forall \tilde{\boldsymbol{u}}_{\mu} \in \tilde{\mathcal{V}}_{\mu}^{(1)}. \tag{11}$$

It may also be shown that for infinitesimal strains and linear elastic constitutive behavior, the following expression for the homogenized stiffness tensor can be derived (Nakshatrala et al 2013; Wallin and Tortorelli 2020):

$$C_{ijkl}^{H} = \frac{1}{|\Omega_{\mu}|} \int_{\Omega_{\mu}} C_{\mu pqrs} \left(\varepsilon_{pq}^{0(ij)} - \varepsilon_{pq}^{*(ij)} \right) \left(\varepsilon_{rs}^{0(kl)} - \varepsilon_{rs}^{*(kl)} \right) dV$$
(12)

for the prescribed microscale unit strain $\varepsilon_{pq}^{0(ij)}$. The local strain field $\varepsilon_{pq}^{*(ij)}$ is derived from (11).

The macroscale system response is then evaluated through the finite element assembly of the element stiffness matrix

$$\mathbf{k}_{\mathrm{M}_{e}} = \int_{\Omega_{\mathrm{M}_{e}}} \mathbf{B}^{T} \mathbf{C}^{H} \mathbf{B} dV_{e}, \tag{13}$$

for the strain-displacement relation B. In (13), we have assumed that the material properties in each macroscale element are the first-order homogenized constitutive relation from (12). After assembly of the global stiffness matrix $K_{\rm M}$, the macroscale deformation $u_{\rm M}$ is evaluated through the expression of linear elastic equilibrium,

$$K_{\mathbf{M}}u_{\mathbf{M}} = f_{\mathbf{M}},\tag{14}$$

for the finite element forcing term $f_{\rm M}$. The macroscale stress is then approximated using the material properties of the solid microarchitecture C_0 and the appropriate element displacement $u_{\rm Me}$ such that

$$\sigma_{M0} = C_0 B u_{Me}. \tag{15}$$

This definition of stress follows from density-based, stress-driven optimization techniques (Duysinx and Bendsøe 1998; da Silva et al 2021a). Critically, σ_{M0} does not capture any amplification effects caused by the local microstructure. Therefore, we implement a local analysis procedure for each microstructure to incorporate local stress effects.

2.2 Second-order microstructure response

The local microstructural response is evaluated using a second-order homogenization approach (Kouznetsova et al 2002, 2004). Deformation in the microscale is considered a function of the strain and strain derivative at the macroscale, as in

$$\Delta x = F_{\mathrm{M}} \cdot \Delta X + \frac{1}{2} \Delta X \cdot \mathbb{G}_{\mathrm{M}} \cdot \Delta X + \mathcal{O}(\Delta X^{3}). \tag{16}$$

for the generic material vector Δx in the deformed configuration, the generic material vector ΔX in the undeformed configuration, and gradient of the deformation gradient

$$\mathbb{G}_{\mathrm{M}} = \nabla F_{\mathrm{M}} = \frac{1}{2} \left(\frac{\partial F_{ij_{\mathrm{M}}}}{\partial X_{k}} + \frac{\partial F_{ik_{\mathrm{M}}}}{\partial X_{i}} \right). \tag{17}$$

The second-order term $\mathbb{G}_{\mathbf{M}}$ establishes a microscale strain that varies with \mathbf{y} as a result of the macroscale deformation. The second-order relations, therefore, slightly relax the strict separation of scales present in first-order homogenization (Kouznetsova et al 2004). This relaxation is important for our work, as we seek a multiscale model with realizable microstructure designs.



The second-order microscale deformation (assuming infinitesimal strains) is therefore expressed as

$$u_{\mu}(y) = u_{M}(x) + \nabla_{x}u_{M}(x) \cdot y$$
$$+ \frac{1}{2} \mathbb{G}_{M} : y \otimes y + \tilde{u}_{\mu}(y)$$
 (18)

Periodic boundary conditions are implemented to further restrict the space of admissible microscale displacements. Following (Kouznetsova et al 2004), two constraints are applied to enforce periodicity within the space defined by (18): the first constraint was defined in (8), and the second constraint restricts fluctuations along Γ^-

$$\int_{\Gamma^{-}} \tilde{\boldsymbol{u}}_{\mu}(\mathbf{y}^{-}) dA = \mathbf{0} \tag{19}$$

to enforce kinematic homogenization of the second-order macroscale strain gradient \mathbb{G}_{M} . The space of kinematically admissible microscale fluctuations

$$\begin{split} \tilde{\mathcal{V}}_{\mu}^{(2)} &= \left\{ \tilde{\boldsymbol{u}}_{\mu} \in \boldsymbol{H}^{1}, \\ \tilde{\boldsymbol{u}}_{\mu}(\mathbf{y}^{-}) &= \tilde{\boldsymbol{u}}_{\mu}(\mathbf{y}^{+}), \quad \int_{\Gamma^{-}} \tilde{\boldsymbol{u}}_{\mu}(\mathbf{y}^{-}) dA = \boldsymbol{0} \right\} \end{split} \tag{20}$$

and the microscale equilibrium condition defined by

$$0 = \int_{\Omega_{\mu}} \boldsymbol{\sigma}_{\mu} : \nabla_{y} \delta \tilde{\boldsymbol{u}}_{\mu} dV \quad \forall \tilde{\boldsymbol{u}}_{\mu} \in \tilde{\mathcal{V}}_{\mu}^{(2)}. \tag{21}$$

follow from the second-order behavior (18) and constraints (8) and (19).

We consider an uncoupled second-order behavior where the macroscale behavior (Fig. 2a) is assumed to be firstorder (Cauchy) material that is unchanged by the microscale second-order response (Fig. 2b). In this approximation of second-order homogenization, the deformation gradient $F_{\rm M}$ and the gradient of the deformation gradient \mathbb{G}_{M} are approximated using the finite element shape functions. Using quadratic elements, these values are readily available (Nguyen et al 2013). These approximations neglect the higher-order stresses in the macroscale but decrease the computational cost of the macroscale analysis because a C^1 continuous finite element scheme is not required (Rodrigues Lopes and Andrade Pires 2022). The effects of these assumptions are a focus in subsequent sections. For a detailed examination of second-order homogenization techniques, readers are directed to Blanco et al (2016a) and Rodrigues Lopes and Andrade Pires (2022).

The second-order microstructure response response u_{μ} is used to evaluate the local stress in each microstructure:

$$\sigma_{\mu} = C_0 B u_{\mu_{\rho}}.\tag{22}$$



where $F_{\rm M}$ and $\mathbb{G}_{\rm M}$ were evaluated at the macro element's centroid and used to calculate u_{μ} using the uncoupled second-order approach. Then the stress-amplification caused by the microarchitecture follows

$$f_a = \frac{\max\left(\sigma_{\mu}\right)}{\sigma_{M0}},\tag{23}$$

where max (σ_{μ}) is the maximum stress within the microstructure (Fig. 3). By definition, $f_a > 1$ for non-solid microstructures.

In summary of the multiscale analysis procedure, a hierarchical structure (Fig. 1a) is decomposed into its microstructures which are homogenized using (12) (Fig. 1b). The homogenized macroscale domain Fig. 1b is analyzed using quadratic finite elements cf. (14). Then the uncoupled second-order microscale analysis is performed (Fig. 2), driven by $F_{\rm M}$ and $\mathbb{G}_{\rm M}$ which are approximated using $u_{\rm Me}$ and the appropriate element shape functions. The microscale equilibrium (21) is evaluated while subjected to periodicity constraints defined by (8) and (19). Using the second-order microscale response, local stresses are evaluated using (22) (Fig. 1d), and the stress amplification in each microstructure is evaluated using (23).

2.3 Evaluation of the second-order scheme

The multiscale analysis formulation presented here relies on multiple simplifying assumptions to configure a model suitable for design optimization. As mentioned previously, the mathematical model for homogenization relies on a separation of macroscale and microscale along with a sufficiently periodic microscale representation (*cf.* (12)). Furthermore, the second-order microscale analysis is uncoupled; higherorder stresses are not considered in the macroscale, instead the macroscale second-order strains are approximated using finite element shape functions (*cf.* Fig. 3). This section illustrates the effects of these assumptions through a comparative study.

To quantify the impact of these assumptions in the multiscale model, a case study was performed to compare four different structural analyses. The four cases, shown in Fig. 4, show (1) poor scale separation with periodic microarchitecture, (2) poor scale separation with random microarchitecture, (3) good scale separation with periodic microarchitecture, and (4) good scale separation with random microarchitecture. Here poor scale separation is characterized by a characteristic ratio of l/L = 0.1 (i.e., 20×10 mesh) for the size of each microstructure relative to the characteristic length of the structure, while good scale separation is characterized by a size ratio of l/L = 0.05 (i.e., 40×20 mesh). The cases introduce elliptical microstructures in 64×64 discretizations of solid (E = 1, v = 0.3) and void

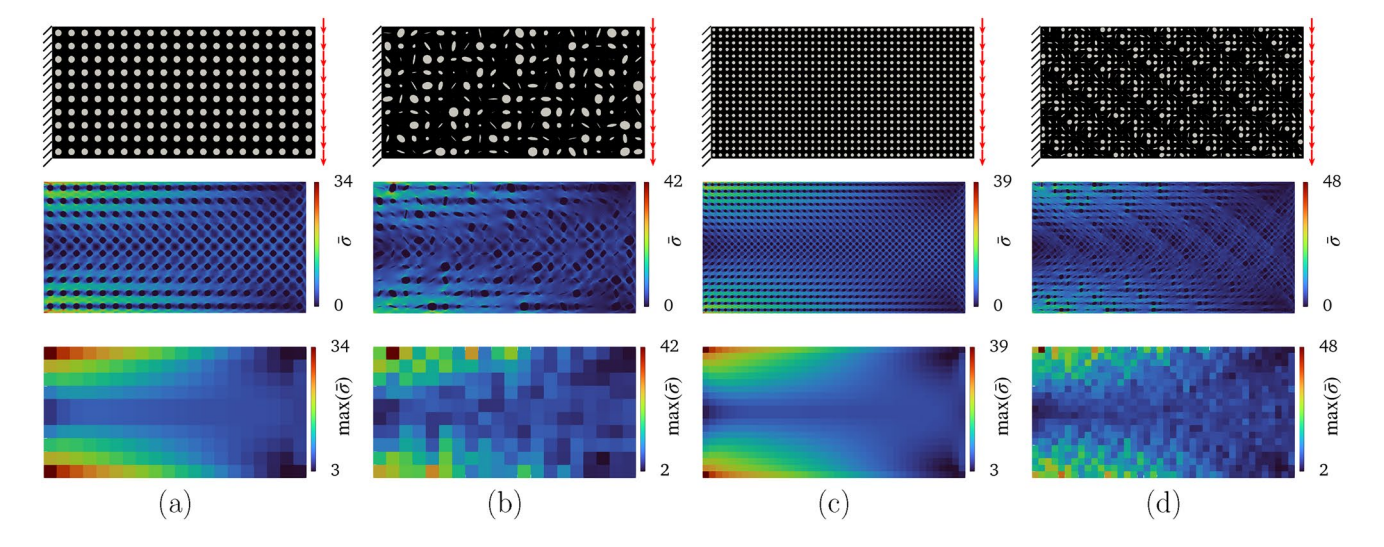


Fig. 4 Four pedagogical cases are considered to evaluate the multiscale model including a l/L=0.1 with periodic microstructures, **b** l/L=0.1 with random microstructures, **c** l/L=0.05 with periodic microstructures, and **d** l/L=0.05 with random microstructures. Mov-

ing row-wise, the plots indicate the material and boundary conditions for each case, the von Mises stress evaluated through fullscale finite element analysis, and the maximum von Mises stress in each microstructure

 $(E=10^{-6}, \nu=0.3)$ material. Each case is constrained on one surface with a distributed load $(|f_{\rm M}||=1)$ along the opposite surface.

A von Mises yield criterion is used in this work and is calculated using

$$\hat{\sigma}_e = \sqrt{\sigma_e^T M \sigma_e} \tag{24}$$

with the matrix

$$\mathbf{M} = \begin{bmatrix} 1 & -\frac{1}{2} & 0 \\ -\frac{1}{2} & 1 & 0 \\ 0 & 0 & 3 \end{bmatrix} \tag{25}$$

defined for plane-stress conditions evaluated at the element centroid and $\sigma_e = \{\sigma_{11}, \sigma_{22}, \sigma_{12}\}_e$. Finite element analysis is performed on a mesh of uniform, quadratic, plane-stress quadrilateral elements. We apply a filter (in the style of density-based topology optimization) for element-wise smoothing of the von Mises stress to limit the effects of the non-conforming mesh, as discussed in more in Sect. 3. For an element i and filter radius ζ , the elements j within that radius are defined as those whose centroid falls within ζ to the centroid of i Bruns and Tortorelli (2001). The centroid-centroid distance d_j is used in a Gaussian-weighted kernel for each element-wise variable α ,

$$\bar{\alpha}_i = \sum_j \frac{\omega_j}{\omega} \alpha_j \tag{26}$$

$$\omega_j = \max\left(1 - \frac{d_j}{\zeta}, 0\right) \tag{27}$$

$$\omega = \sum_{j} \omega_{j},\tag{28}$$

which will produce the "smoothed" quantity $\bar{\alpha}$. The von Mises stress in Fig. 4 is $\bar{\sigma}$, the smoothed von Mises stress is filtered using ζ equal to three times the microscale element's width.

The von Mises stress for the four test cases is shown in Fig. 4. The fullscale stress is evaluated using a fully realized discretization: 1280×640 elements in the case of l/L = 0.1 and 2560×1280 in the case of l/L = 0.05. The maximum von Mises stress in each microstructure is also shown and is related to the stress amplification caused by the microarchtiecture (cf. (23)).

The fullscale von Mises stress is compared to homogenization techniques in Fig. 5; first-order evaluation of the local stress ($\mathbb{G}_{M}=0$) is compared to the equivalent second-order analysis. Error is calculated using the relative error norm measured relative to the fullscale analysis:

error =
$$\frac{||x_{\text{true}} - x_{\text{approx.}}||_2}{||x_{\text{true}}||_2}$$
 (29)

As a consequence of poor scale separation, (Fig. 5a, b), the homogenized material model used to calculate $F_{\rm M}$ and $\mathbb{G}_{\rm M}$ is inaccurate. This error propagates to the calculation of local stress within Ω_{μ} . The error is especially evident near the boundaries of $\Omega_{\rm M}$ where the homogenized material model



fails to capture the effects of the boundary conditions. As scale separation improves (Fig. 5c, d), the homogenized material model becomes more accurate, and both homogenization methods improve. For random microarchitectures, error is induced regardless of the scale separation.

In all cases, the second-order approach significantly reduces the error in the microscale analysis, especially near the boundary of $\Omega_{\rm M}$ (Table 1). We note that in situations where the microstructure is sufficiently periodic with poor scale separation (e.g., Fig. 5a), the second-order homogenization approach significantly reduces the error in the von Mises stress recovery. Stress along the microstructural boundaries, in addition to the maximum stress in each microstructure, is more accurately modeled with the second-order homogenization approach.

Table 1 The relative error norm of the von Mises stress $\bar{\sigma}$ is recorded for the four test cases shown in Fig. 5

Case	1 st Order	2 nd Order
(a) $l/L = 0.1$; Periodic	0.125	0.075
(b) $l/L = 0.1$; Random	0.178	0.137
(c) $l/L = 0.05$; Periodic	0.079	0.061
(d) $l/L = 0.05$; Random	0.148	0.127

3 Machine learning surrogate modeling

The multiscale formulation presented previously relies on two independent microstructure analyses (*cf.* Fig. 1). The first step involves the evaluation of effective material properties through (12), and the second step evaluates local stresses through a second-order scheme (*cf.* (22)). While Table 1 shows a reasonable accuracy for this approach, the computational cost of these successive unit cell analyses is undesirable for design optimization which may require hundreds of iterations to converge. Therefore, we seek an efficient surrogate model for both the evaluation of effective material properties and the evaluation of local stresses.

Three parameterized microstructures are considered for the multiscale stress-constrained design of hierarchical structures. Design parameters are defined by a vector α_e for each macroscale element. The first is an elliptical inclusion defined by three parameters: major axis radius r_1 , minor axis radius, r_2 , and major axis rotation from the horizontal θ , so $\alpha_e = \{r_1, r_2, \theta\}$ (Fig. 6). The elliptical shape naturally limits the stress concentrations introduced in the microstructure. The second microstructure is a truss parameterized by effective density, so $\alpha_e = \{\rho\}$ (Fig. 7). This truss mimics similar microstructures that approach the Hashin-Shtrikman (HS) bounds for two-phase materials (Träff et al 2018). The next

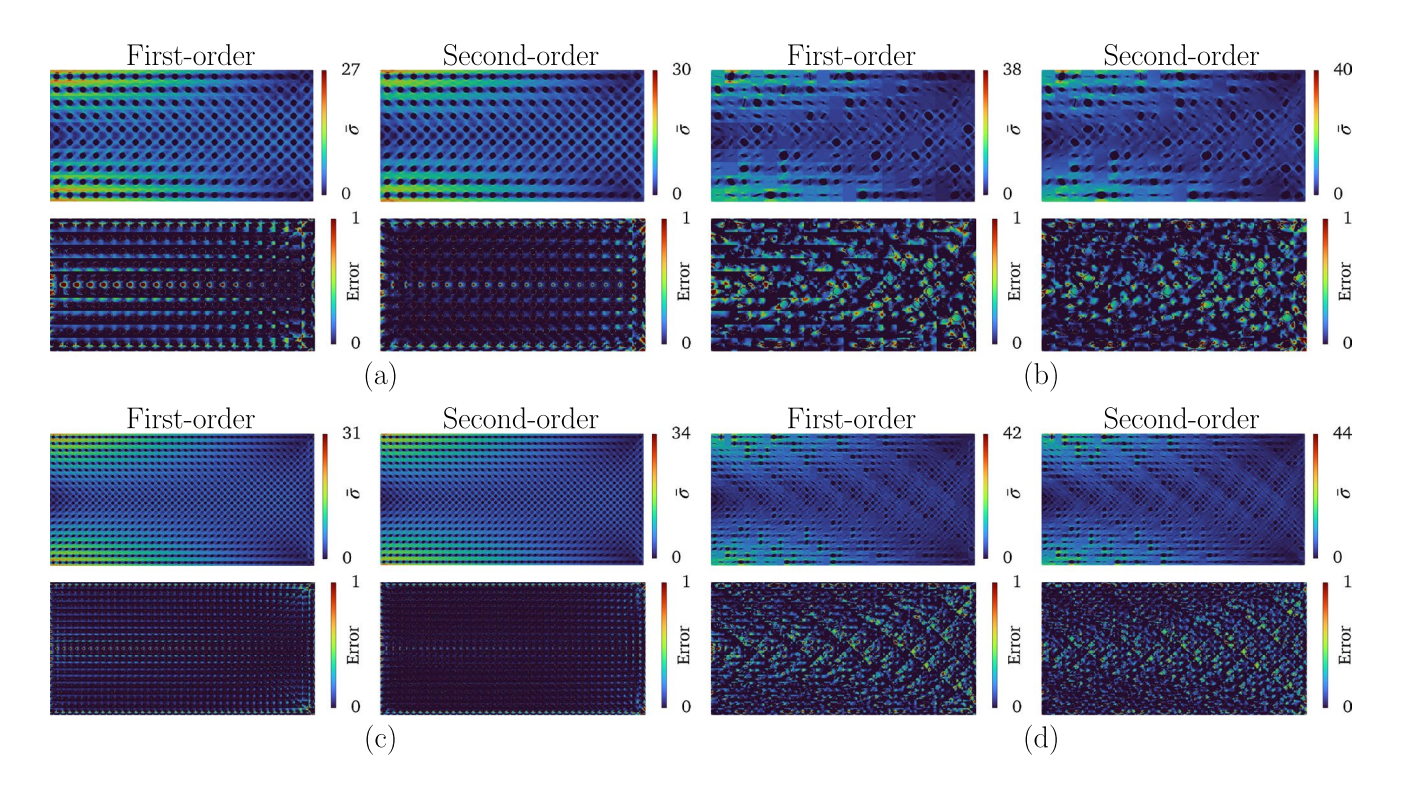


Fig. 5 The four pedagogical examples introduced in Fig. 4 are evaluated using first-order and second-order homogenization of the microstructures. The von Mises stress, evaluated for each microstructure

then plotted on the macroscale mesh, is shown in addition to its error measured relative to fullscale analysis



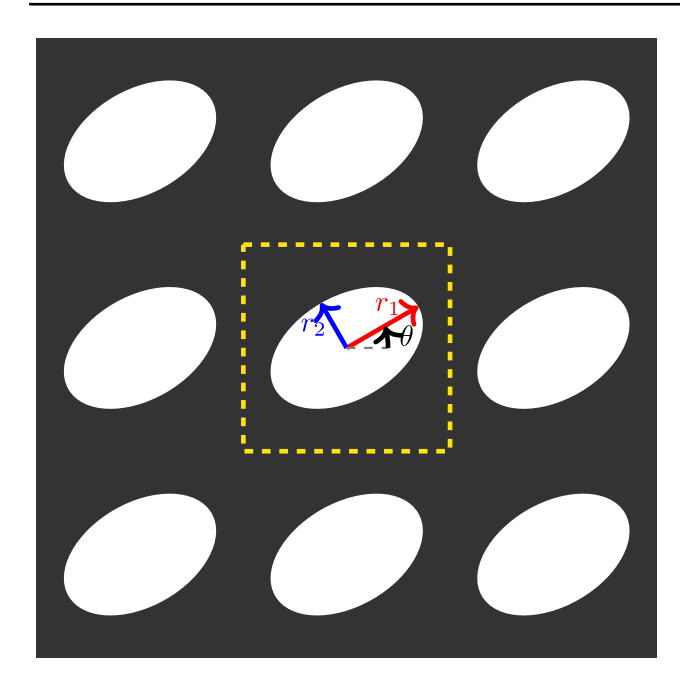


Fig. 6 The ellipse microarchitecture is parameterized by three design variables (r_1, r_2, θ) , and the unit cell is highlighted here within a 3×3 array of architectures

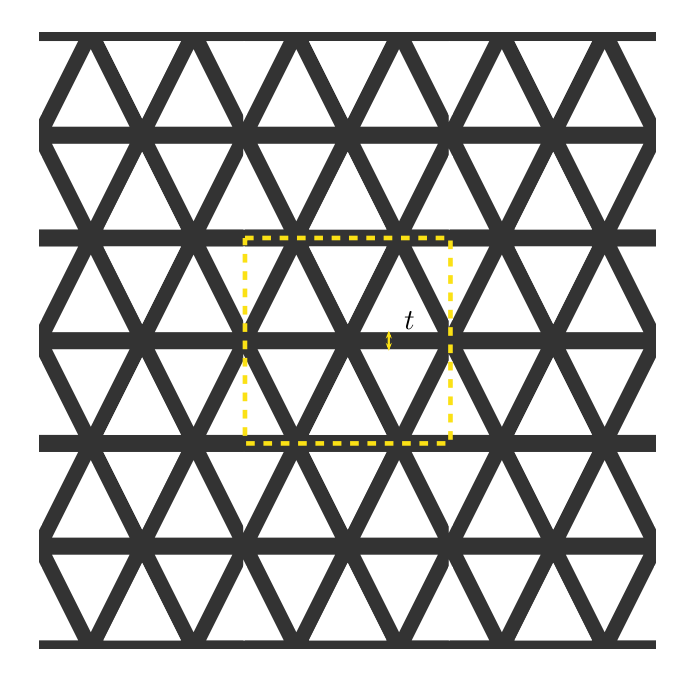


Fig. 7 The HS-truss microarchitecture is parameterized by its effective density ($\rho = 1 - 4(0.5 - 3t)^2$, and the unit cell is highlighted here within a 3×3 array of architectures

microstructure design is a 2D biotruss design named because of its organically shaped inclusions (Fig. 8). The surfaces of the biotruss are parameterized using four independent bézier curves resulting in 10 geometric parameters per microarchitecture (Black and Najafi 2023). All microstructures are

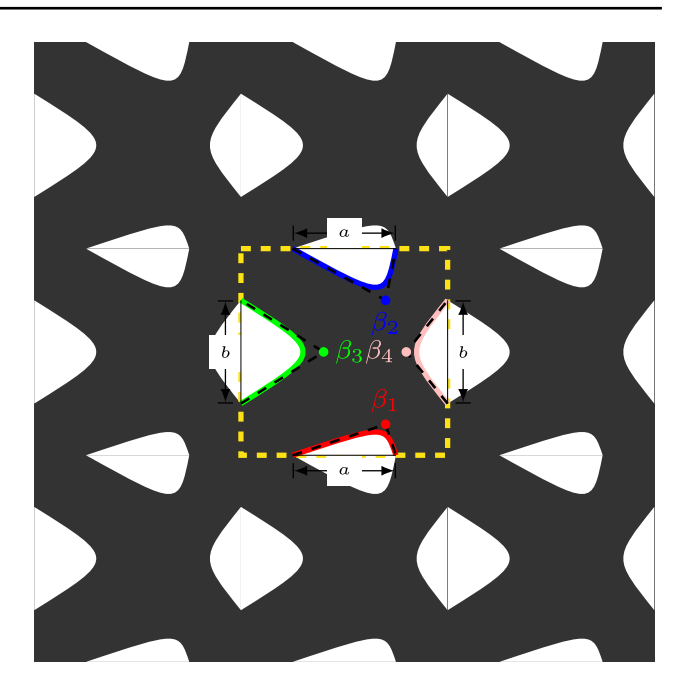


Fig. 8 The biotruss microarchitecture is parameterized by four bézier curves (10 total parameters), and the unit cell is highlighted here within a 3×3 array of architectures

defined by a uniform 64×64 discretization of solid (E = 1, v = 0.3) and void ($E = 10^{-6}$, v = 0.3) material.

The neural network is considered for surrogate model development (Fig. 9). The neural network has shown to be an effective, efficient surrogate model for homogenization (White et al 2018; Black and Najafi 2023). When trained effectively, that is without overfitting, vanishing/exploding gradients, etc., the neural network's jacobian has proven valuable in the design optimization process (Black and Najafi 2023). Two neural network models will be presented as surrogate for the aforementioned (1) evaluation of the microstructure's effective material properties and (2) evaluation of local stresses using a second-order scheme.

The first class of neural network was trained to estimate the homogenized constitutive properties (cf. (12)) for each of the parameterized unit cell design (Figs. 6, 7, 8). We implement a similar formulation to Black and Najafi (2023) with a 3 hidden layer, 64 neuron network with sigmoid activations that produces the independent components of C^H based on the microstructure's design parameter input. In summary, the first class of neural network maps the microstructure's geometric parameters to its homogenized properties:

$$DNN_1(\boldsymbol{\alpha}_e) \approx \boldsymbol{C}^H. \tag{30}$$

For all three microstructure designs, this class of network was trained using 667 random input and their resulting output produced via finite element analysis and computational homogenization of the unit cell design via (12). Using a



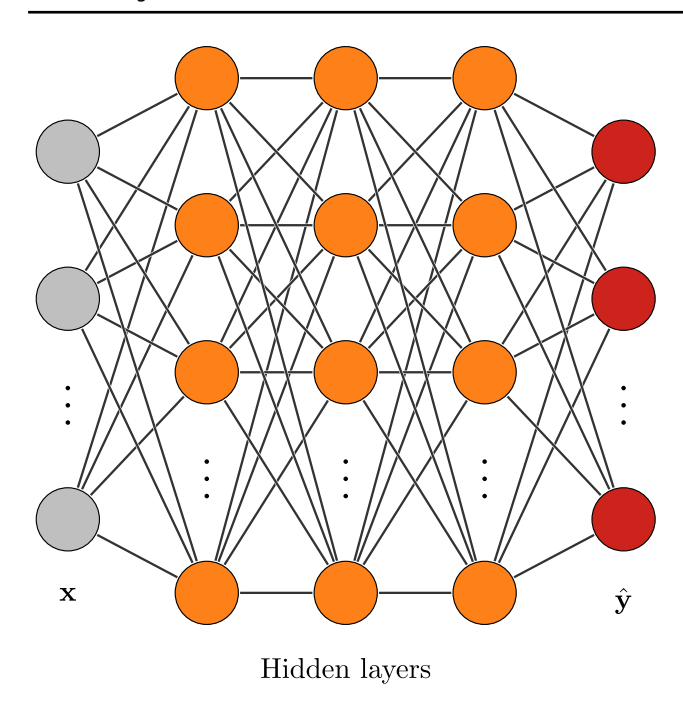


Fig. 9 The neural network maps an input vector x to an output vector \hat{y} through a series of hidden layers. Three hidden layers are shown here, each characterized by a number of neurons shown as connected nodes

mean squared error objective function over 1,000 epochs of training with the Adam optimizer (Kingma and Ba 2017), randomized batches of 8 training examples, and a learning rate of 10⁻³, the network converged to a relative root mean squared error (RRMSE) less than 0.05 for all unit cell designs (Fig. 10) measured on 333 validation examples.

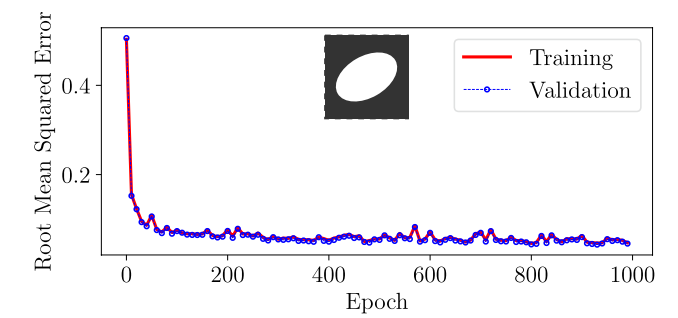
The second class of neural network was trained to approximate the von Mises stress amplification factor (cf. (23)). The input for this class of neural network is the parameterized microstructure geometry and the normalized macroscale displacement value u_{Me} . The amplification factor in these cases is calculated using the maximum local von Mises stress and the macroscale solid stress:

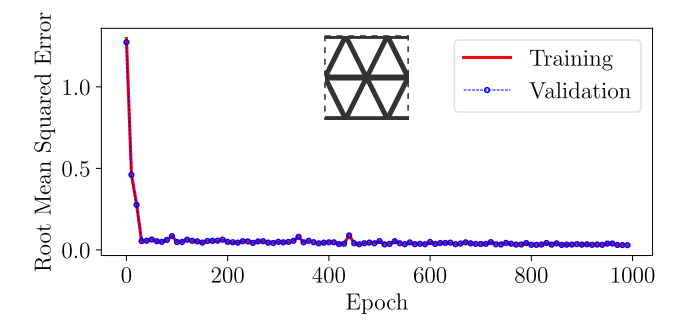
$$\hat{f}_a = \frac{\max(\bar{\sigma}_{\mu}^e) \in \Omega_{\mu}}{\hat{\sigma}_{M_0}}.$$
(31)

The normalized displacement input is mapped to its strain and strain derivative at the microstructure centroid, then the input parameters are passed through a 3 hidden layer, 64 neuron network with sigmoid activations that is trained to predict \hat{f}_a , so

$$DNN_2(\boldsymbol{\alpha}_e, \boldsymbol{u}_{Me}) \approx \hat{f}_a. \tag{32}$$

Training data is generated using the second-order homogenization scheme (cf. (16)) with randomized inputs. This class





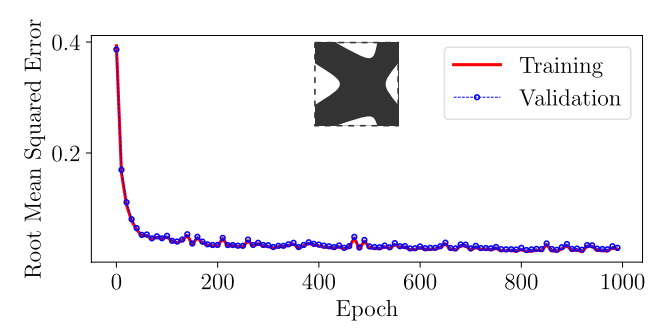


Fig. 10 Convergence of the neural network surrogate model for evaluating the components of the homogenized constitutive tensor is shown for three microstructure designs

of network is trained on 6,660 examples over 1,000 epochs with batches of 8 examples and a learning rate of 10^{-3} . The larger training dataset was required to capture the larger input space (which now incorporates the space of macroscale displacements u_{Me}). The resulting networks achieved a RRMSE of less than 0.1 for all three design cases (Fig. 11).

The performance of the neural networks trained to evaluate effective material properties and local stress amplification in the ellipse microstructure is evaluated using the four pedagogical examples originally presented in Fig. 4. The maximum stress in each microstructure as evaluated by full-scale finite element analysis, a macroscale approximation of stress (15) through second-order homogenization *cf.* (16), and the neural network surrogate models (31) are compared in Fig. 12. The relative error norm for these cases is also compared in Table 2.

The error presented in Table 2, measured relative to the full scale finite element evaluation of $\bar{\sigma}$ (the von Mises stress



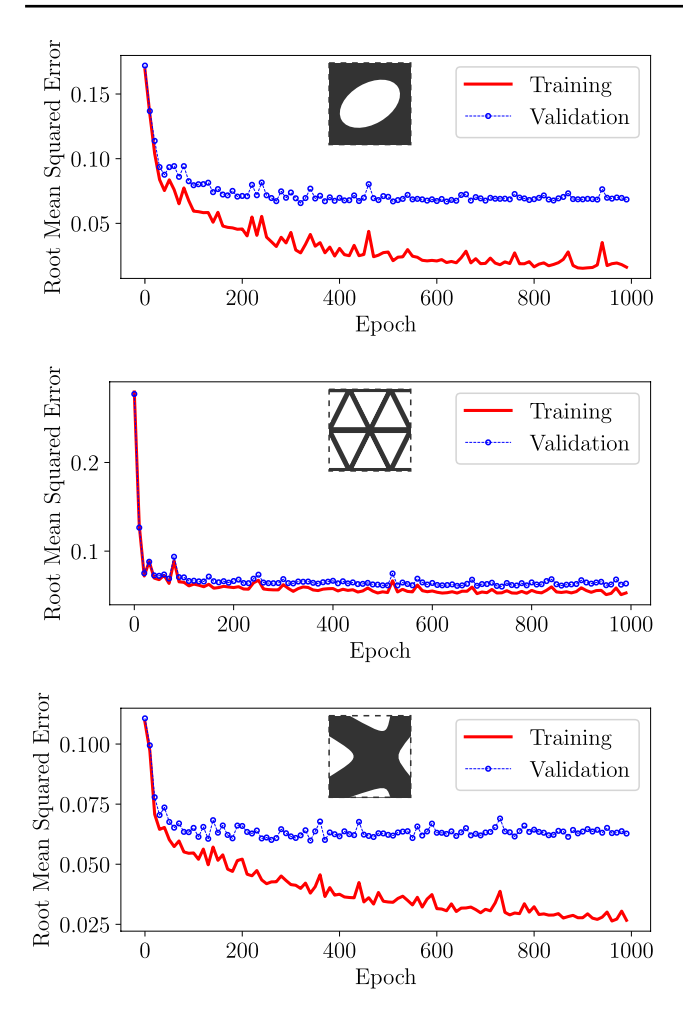


Fig. 11 Convergence of the neural network surrogate model for evaluating the stress amplification modeled by second-order homogenization is shown for three microstructure designs

at each "micro" element centroid), illustrates the practical effects of the homogenization-based multiscale modeling approach. When predicting the maximum stress in each microstructure, two deep neural network (DNN) surrogates model are trained to predict (1) the homogenized constitutive tensor of the microarchitecture and (2) the maximum stress within the microarchitecture as modeled by second-order homogenization techniques. As discussed in the previous section, both of these homogenization techniques rely on some assumptions related to the separation of scales and periodicity of the microstructure. These assumptions induce error which is compounded by the error in the neural network surrogate model. The resulting approach yields a prediction of the maximum stress within 10–15% of the ground truth.

Compared to either a fullscale evaluation of the structure (which scales poorly with the size and complexity of the hierarchical structure) or a homogenization approach (which relies on successive evaluations of each unit cell), the neural network surrogate model approach has yielded 1,000-10,000 times faster evaluations. This evaluation time is pertinent to the overall computational cost of the multiscale evaluation as each microstructure in the macroscale domain must be analyzed. As the problems scale, the cost of these nested evaluations becomes untenable. The cost of data generation (1,000 examples for the surrogate of homogenized constitutive tensors and 10,000 examples for the surrogate of second-order evaluation of stress amplification) is relatively small; the training data for this work was generated in approximately one hour on (Intel i7 @4.1 GHz on 4 cores). Furthermore, the neural network surrogate models are suitable for optimization, as each mapping's jacobian may be recovered through backpropagation. Although this jacobian is not necessarily as accurate as the evaluation accuracy, it has shown to be effective and useful in design optimization scenarios (Black and Najafi 2023).

4 Optimization formulation

This section presents a formulation for multiscale stress-constrained design using the neural network surrogate models to predict stress amplification. For a multiscale structure composed of many spatially varying microarchitectures, we seek a design framework that limits the maximum local von Mises stress within each microstructure. The multiscale design optimization framework must consider design variables in both the macro- and microscales. The formulation presented here applies a density variable ρ to define the macroscale topology. Each microstructure in the macroscale domain is assigned $\rho_e \in (0, 1]$ to indicate the presence of a microstructure. The centroid of each macroscale element is used to characterize each microstructure, ρ_e is defined for each of the M macroscale elements. Each microarchitecture is defined by a set of parameters α_e that fully described the local geometry. For example, the elliptical microstructure presented in Sect. 3 is parameterized by $\alpha_e = \{r_1, r_2, \theta\}$ to define the elliptical inclusion in each microarchitecture.

The neural network surrogate models for homogenized constitutive properties and local stress evaluation presented in Sect. 3 are integrated into the optimization formulation. The effective properties of each microstructure are defined in terms of the filtered macroscale density and the microstructure design parameters such that

$$C_{\text{Me}}(\bar{\rho}_e, \bar{\alpha}_e) = \left(\rho_{\text{min}} + (1 - \rho_{\text{min}})\bar{\rho}_e^p\right) \left(\hat{\boldsymbol{C}}^H(\bar{\alpha}_e)\right)$$
(33)

for a minimum density $\rho_{\min} = 10^{-6}$, penalization parameter p = 3 (Zhou and Rozvany 1991; Rozvany et al 1992), and neural network prediction of the homogenized constitutive tensor \hat{C}^H . Each design variable (ρ_e, α_e) is filtered using (26), and the macroscale layout variable ρ is further projected using (Wang et al 2011)



102 Page 12 of 23 N. Black, A. Najafi

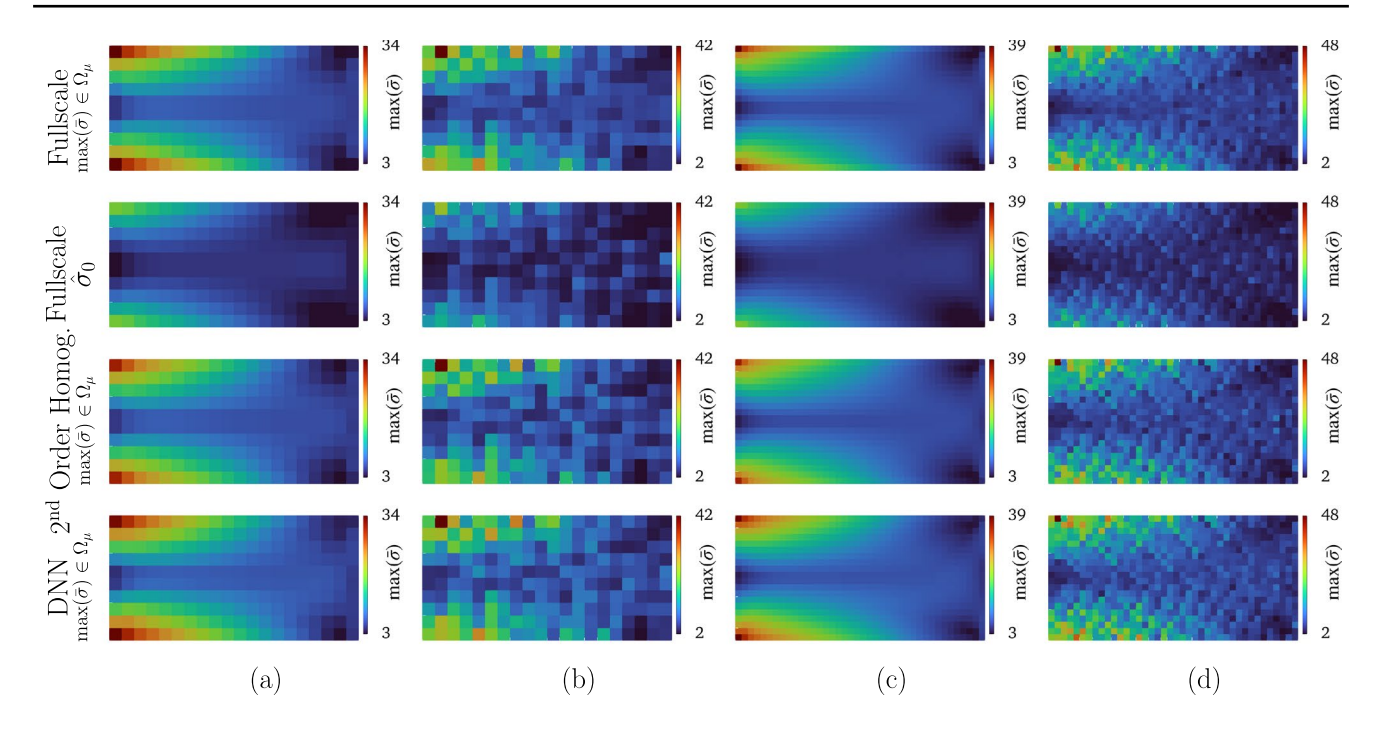


Fig. 12 The maximum stress in each microstructure is compared for multiple strategies shown row-wise for the four pedagogical test cases of Fig. 4: the stress evaluated from fullscale finite element analysis, the stress evaluated using the macroscale deformation and a solid,

isotropic material model, the maximum stress evaluated via secondorder homogenization of each microstructure, and the result of the neural network surrogate approach

Table 2 The relative error norm of the maximum microstructural von Mises stress $\max(\bar{\sigma}) \in \Omega_m$ is recorded for the four test cases shown in Fig. 5

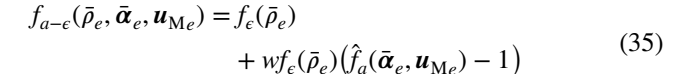
Case	$\hat{\sigma}_0$	1 st Order	2 nd Order	DNN (Speedup: $\approx 10^4$)
(a) $l/L = 0.1$; Periodic	0.390	0.105	0.061	0.079
(b) $l/L = 0.1$; Random	0.419	0.155	0.122	0.148
(c) $l/L = 0.05$; Periodic	0.362	0.065	0.046	0.096
(d) $l/L = 0.05$; Random	0.397	0.124	0.105	0.176

Here we also note that the speedup in homogenization and local stress evaluation for the DNN is on the order of 10^4 (measured on a single core)

$$\bar{\rho}_e = \frac{\tanh(\beta \eta) + \tanh(\beta (\tilde{\rho}_e - \eta))}{\tanh(\beta \eta) + \tanh(\beta (1 - \eta))}$$
(34)

where $\tilde{\rho}_e$ represents the filtered density variable in each element, β is varied throughout the optimization to penalize intermediate densities, and $\eta = 0.5$ in this work.

The stress amplification function (31) is approximated using the second class of neural network as $\hat{f}_a(\bar{\alpha}_e, u_{\text{M}e})$. To avoid the singularity phenomenon as $\rho_e \to 0$, the stress amplification is also combined with stress interpolation (Cheng and Guo 1997; Duysinx and Sigmund 1998) in a combined interpolation-amplification function



where

$$f_{\epsilon}(\bar{\rho}_{e}) = \frac{\bar{\rho}_{e}}{\epsilon(1 - \bar{\rho}_{e}) + \bar{\rho}_{e}} \tag{36}$$

with $\epsilon = 0.2$. The parameter $w \in [0, 1]$ is an optional weighting parameter for the stress amplification that is varied throughout the optimization. The amplification function (35) has been introduced in this work to control the optimization's sensitivity to local stress amplification. If w = 0, the amplifications caused by microstructural geometries are neglected. If w = 1, the stress is amplified by the local amplification factor.

Stress constraints are expressed for each microstructure (i.e., each macroscale element) via

$$\frac{f_{a-\epsilon}(\bar{\rho}_e, \bar{\boldsymbol{\alpha}}_e, \boldsymbol{u}_{\mathrm{M}_e})\hat{\sigma}_0(\boldsymbol{u}_{\mathrm{M}_e})}{\sigma_Y} - 1 < 0 \quad e = 1, 2, ..., M, \tag{37}$$

for the von Mises yield stress σ_Y . The stress constraints, therefore, define a limit of the maximum von Mises stress within each microstructure of the domain; they depend on the macroscale layout ρ_e , microarchitecture geometric parameters α_e , and macroscale response u_M .



The objective of the optimization is to minimize the volume/mass of a multiscale structure subjected to stress constraints in each microstructure. The optimization formulation is defined as

$$\min_{\rho,\alpha} \Theta = \frac{1}{M} \sum_{e=1}^{M} v_e(\rho_e, \alpha_e),$$
s.t.: $K_{\rm M} u_{\rm M} = f_{\rm M}$,
and: $\rho_{\rm min} < \rho_e < \rho_{\rm max}$,
$$\alpha_{\rm min} < \alpha_e < \alpha_{\rm max},$$

$$\frac{f_{a-\epsilon}(\bar{\rho}_e, \bar{\alpha}_e, u_{\rm Me})\hat{\sigma}_0(u_{\rm Me})}{\sigma_Y} - 1 < 0,$$

$$e = 1...M.$$
(38)

The structure's volume is introduced in (38) where $v_e(\rho_e, \alpha_e)$ is the volume fraction of solid material in each microstructure defined as

$$v_e(\rho_e, \boldsymbol{\alpha}_e) = \rho_e v_\alpha(\boldsymbol{\alpha}_e) \tag{39}$$

and v_{α} is the volume fraction of the each microstructure. Based on these definitions, additional volume constraints may be appended to the optimization problem including a constraint of the macrostructural layout

$$\frac{1}{M} \sum_{e=1}^{M} \rho_e - V_{\rho} < 0 \tag{40}$$

and a constraint of the average microstructural infill

$$\frac{1}{\sum_{e=1}^{M} \rho_e} \sum_{e=1}^{M} v_e(\rho_e, \alpha_e) - V_\alpha < 0 \tag{41}$$

for the target values V_a and V_a (summarized in Fig. 13).

The augmented lagrangian method is implemented to handle the large number of inequality constraints related to the local stress constraints (Ito and Kunisch 1990). The objective function is redefined in the manner of da Silva et al (2021a):

$$\Theta = \frac{1}{M} \sum_{e=1}^{M} v_e(\rho_e, \boldsymbol{\alpha}_e)$$

$$+ \frac{r}{2} \sum_{e=1}^{M} \langle \frac{\mu_e}{r} + \frac{f_{a-\epsilon}(\bar{\rho}_e, \bar{\boldsymbol{\alpha}}_e, \boldsymbol{u}_{Me}) \hat{\sigma}_0(\boldsymbol{u}_{Me})}{\sigma_Y} - 1 \rangle^2$$

$$(42)$$

with the scaling parameter r and approximate lagrange multiplier μ_e .

Several hyperparameters have been introduced to enforce the local stress constraints including β , w, r, and μ . The parameters β , w, and r are iteratively updated throughout the optimization process using

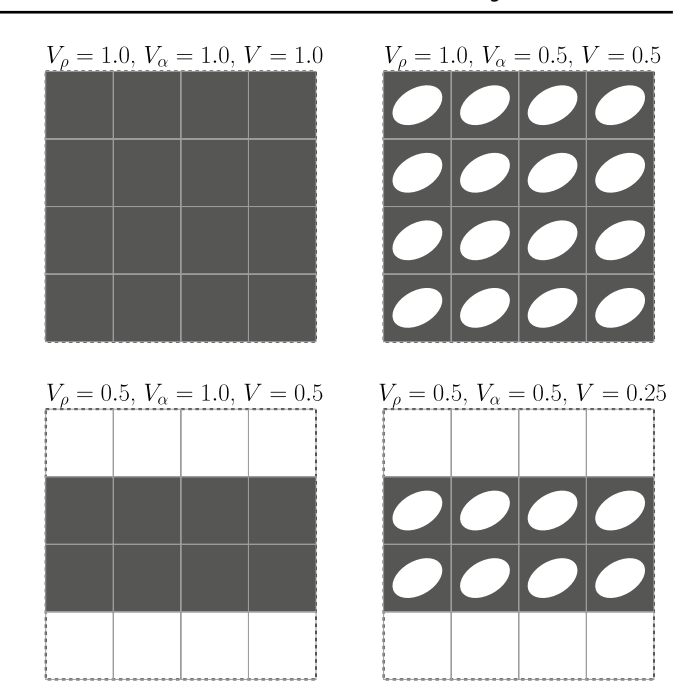


Fig. 13 Four example of hierarchical designs are characterized by three measures of volume fractions: the layout volume V_{ρ} , average microstructural volume V_{α} , and net volume V. The elliptical inclusion shown here is 50% void, so the volume fraction of each microstructure is 50%

$$x^{(i+1)} \leftarrow \max \left\{ x_F, x^{(i)} \left(\frac{x_F}{x_0} \right)^{\frac{1}{N_F/N_i - 1}} \right\}$$
 (43)

for the generic variable x with current value x_i , initial value x_0 , and final value x_F that is updated every N_i iterations for N_F total iterations. The parameter μ , the approximate lagrange multiplier, is updated as

$$\mu_e^{(i+1)} \leftarrow r \left\langle \frac{\mu_e}{r} + \frac{f_{a-\epsilon}(\bar{\rho}_e, \bar{\boldsymbol{\alpha}}_e, \boldsymbol{u}_{\mathrm{M}_e}) \hat{\sigma}_0(\boldsymbol{u}_{\mathrm{M}_e})}{\sigma_Y} - 1 \right\rangle^{(i)}. \tag{44}$$

4.1 Sensitivity analysis

The iterative optimization of the parameterized multiscale structure requires an expression for the objective's gradient with respect to the macroscale design variables $\bar{\rho}$ and microstructure design variables $\bar{\alpha}$. Adjoint sensitivity analysis is employed to derive this sensitivity information. First (42) is modified to

$$\Theta = \frac{1}{M} \sum_{e=1}^{M} v_e(\rho_e, \alpha_e) + \frac{r}{2} \sum_{e=1}^{M} \mathcal{L}^2 + \lambda^T (\mathbf{K}_{\mathrm{M}} \mathbf{u}_{\mathrm{M}} - \mathbf{f}_{\mathrm{M}})$$
(45)



where the simplification $\mathcal{L}=\langle \frac{\mu_e}{r}+\frac{f_{a-e}(\bar{\rho}_e,\bar{\alpha}_e,u_{\rm M_e})\sigma_0(u_{\rm M_e})}{\sigma_\gamma}-1\rangle$ has been introduced and the arbitrary adjoint variable λ has been added given that $K_{\rm M}u_{\rm M}=f_{\rm M}$. To simplify notation, we introduce the generic design variable d which may substitute either $\bar{\rho}_e$ or a component of $\bar{\alpha}_e$. The sensitivity analysis follows

$$\frac{\partial \Theta}{\partial d} = \frac{1}{M} \frac{\partial v_{e}}{\partial d} + \frac{r}{\sigma_{Y}} \mathcal{L}_{e} \left[\frac{\partial f_{a-\epsilon}}{\partial d} (\hat{\sigma}_{0}) + \frac{\partial f_{a-\epsilon}}{\partial u_{Me}} (\hat{\sigma}_{0}) \frac{\partial u_{Me}}{\partial d} + \frac{f_{a-\epsilon}}{\hat{\sigma}_{0}} \left(C_{0} B u_{Me} \right)^{T} M C_{0} B \frac{\partial u_{Me}}{\partial d} \right] + \lambda_{e}^{T} \left(\frac{\partial k_{Me}}{\partial d} u_{Me} + k_{Me} \frac{\partial u_{Me}}{\partial d} \right)$$
(46)

which simplifies to

$$\frac{\partial \Theta}{\partial d} = \frac{1}{M} \frac{\partial v_e}{\partial d} + \frac{r}{\sigma_v} \mathcal{L}_e \frac{\partial f_{a-e}}{\partial d} (\hat{\sigma}_0) + \lambda_e^T \left(\frac{\partial \mathbf{k}_{Me}}{\partial d} \mathbf{u}_{Me} \right)$$
(47)

provided that the adjoint variable is evaluated from the solution of

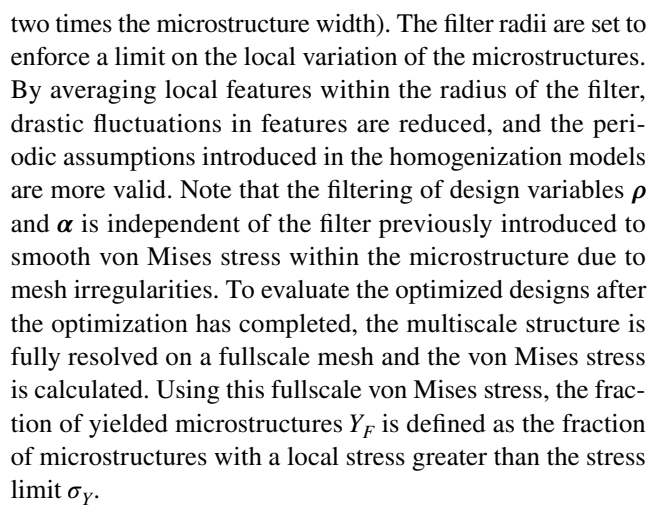
$$K_{\mathrm{M}}\lambda$$

$$= \frac{-r}{\sigma_{Y}} \sum_{e=1}^{M} \mathcal{L}_{e} \left[\frac{\partial f_{a-e}}{\partial u_{\mathrm{M}e}} (\hat{\sigma}_{0}) + \frac{f_{a-e}}{\hat{\sigma}_{0}} \left(\left(C_{0} B u_{\mathrm{M}e} \right)^{T} M C_{0} B \right) \right]. \tag{48}$$

The components $\frac{\partial k_{\text{Me}}}{\partial d}$, $\frac{\partial f_{a-e}}{\partial d}$, and $\frac{\partial f_{a-e}}{\partial u_{\text{Me}}}$, are readily derived from the neural network surrogate models through backpropagation (Black and Najafi 2023).

5 Examples

This section evaluates the stress-constrained multiscale design optimization framework through numerous examples with different boundary conditions and microstructural parameterizations. Depending on the choice of microarchitecture, the appropriate pair of neural networks introduced in Sect. 3 is used in the iterative optimization of (42) using the MMA optimizer (Svanberg 1987). To facilitate fair comparison of optimized designs, the fixed parameter update scheme shown in Table 3 is applied, then the optimization continues for 100 more iterations (500 total iterations). Additionally, filtering is applied via (26) for both the layout variable ρ (filter radius ζ is three times the microstructure width) and microarchitecture variables α (filter radius ζ is



The first set of examples implement the canonical benchmark L-bracket design shown in Fig. 14. Here the reentrant corner introduces a stress concentration that the optimization must rectify. To prevent the boundary sticking phenomena, buffer zones are introduced (with a size equal to the filter radius of ρ) in the manner of da Silva et al (2021a). In each buffer zone, $\rho_e = \rho_{\min}$ and α_e is defined so that the microstructure is completely solid. The domain is discretized into 4096 microstructures resulting in a macroscale mesh of 0.0125×0.0125 quadrilaterals. Each microstructure is then represented by a 64×64 mesh of quadrilaterals. The horizontal 1×0.4 portion of the L-bracket design space in Fig. 14, for example, is represented by an 80×32 mesh of quadrilaterals resulting in a characteristic length l/L = 1/80 = 0.0125. Its "fullscale" equivalent would be a 5120×2048 mesh and is created by resolving each 64×64 microstructure in place of a single macroscale element. As in Sect. 2.3, quadratic 8-node plane stress elements without thickness are used in the macroscale evaluation, while 4-node plane stress elements without thickness are used in the microscale evaluation and subsequent "fullscale" analysis. Each example in this section will use the same elements and discretization strategy with each mesh defined by its characteristic length denoted by ratio of each square microstructure to a unit macroscale length. A stress limit

Table 3 The update strategy for the optimization parameters is presented including the initial value, maximum value, update frequency, and update range

param (see also)	init max x_0 x_F		freq N_i	start-stop (N_0-N_F)	
p (33)	3	3	_	_	
β (34)	0.5	10	20	0-400	
w (35)	0.1	1.0	20	0-400	
r (42)	$\frac{0.01}{M}$	100	20	0-400	
μ (42), (44)	0^{M}	<i>M</i> —	20	0-400	



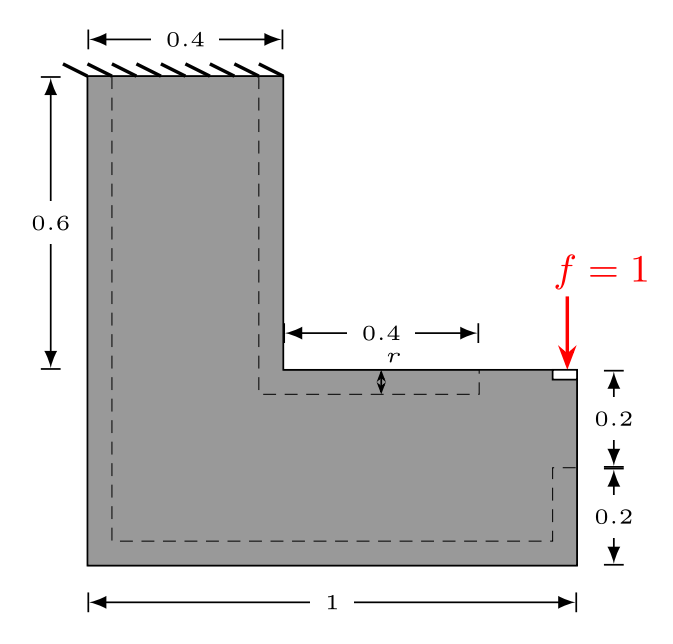
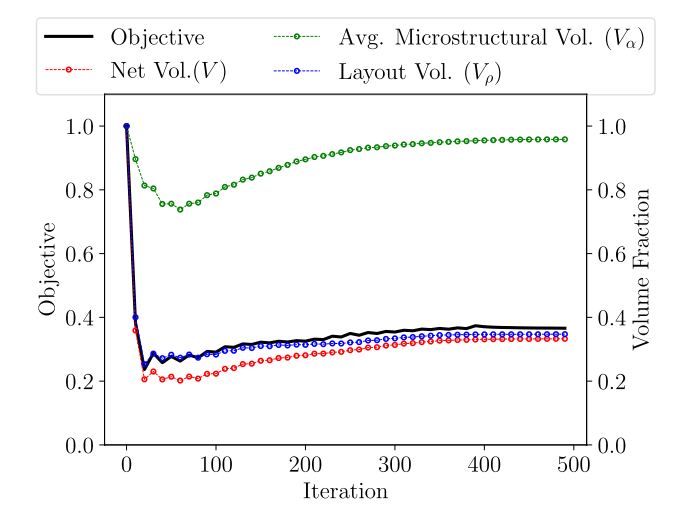


Fig. 14 The L-bracket benchmark boundary conditions are shown including the buffer zone indicated by dashed lines



 $\textbf{Fig. 15} \ \ \textbf{The convergence of the optimized multiscale L-bracket design with elliptical microarchitecture is shown}$

of $\sigma_Y = 75$ is set for the given loading conditions. Figure 15 illustrates the convergence behavior for the elliptical microstructure.

Starting from a solid design $(V_{\alpha} = 1.0)$, the optimization process begins by significantly reducing the structural volume. As shown in Fig. 16, the successive updating of the parameters β , r, w, and μ results in a more stringent evaluation of the stress constraints. The structure's infill is therefore gradually increased, approaching a 96% solid infill and a 33% net volume fraction. The evolution of the objectives and constraints is influenced by the hyperparameters defined in Table 3, especially the weight r defined in (42). In the first 100 iterations, the parameter r is relatively small and scales the objective to penalize structural volume more than violations of the stress constraints. As the optimization progresses, r increases the nominal value of the augmented lagrangian term, resulting in the rising objective value observed in Fig. 15. This effect is compounded by the increasing parameter w which penalizes the local microstructural stress value.

The von Mises stress distribution is further analyzed in Fig. 17. Here a selection of local stress-distributions - obtained through homogenization of each independent unit cell - are contextualized within the "fullscale" stress distribution previously shown in Fig. 16. The cell-level stress distributions are representative of the data used in training the neural network surrogates used in the optimization formulation. Meanwhile, the "fullscale" analysis remains the best model for the response of the structure with observable microstructures, so we use this representation for evaluation of the proposed framework.

Multiscale design optimization, however, is dependent on the initial design configuration, and this framework is no exception. Figures 18 and 19 show the same optimization results for a design initialized with a 74% infill. In this case, the lower infill volume fraction propagates through the optimization, resulting in a final infill volume fraction of 94% and a 37% net volume fraction. The higher volume fraction in this case indicates the presence of local minima, another trait of multiscale design. In both cases of L-bracket

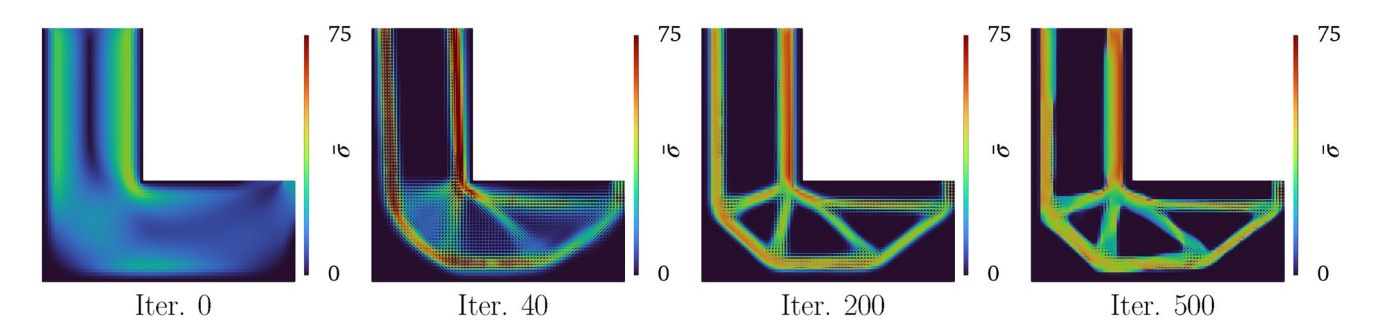


Fig. 16 The von Mises stress $\bar{\sigma}$ evaluated on an equivalent fullscale mesh is shown for the design problem outlined in Fig. 15



102 Page 16 of 23 N. Black, A. Najafi

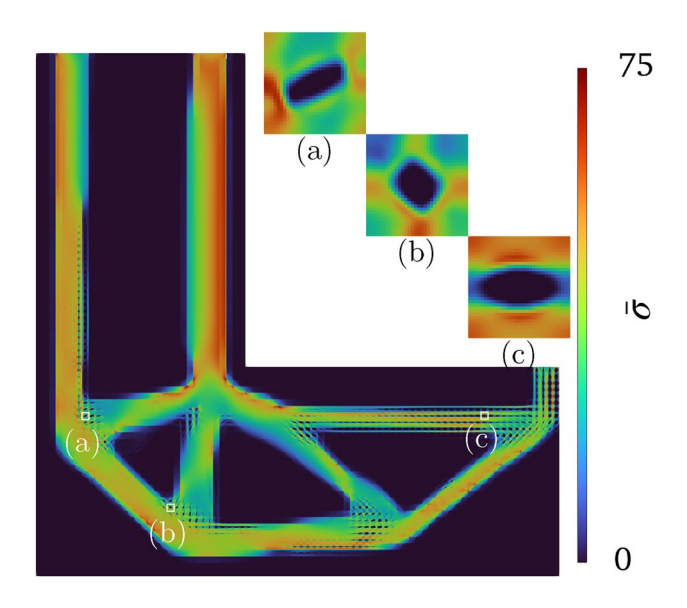


Fig. 17 The von Mises stress $\bar{\sigma}$ is detailed for an equivalent fullscale analysis of the optimized result from Fig. 15. Details **a**–**c** show the results of a multiscale analysis of the same problem where the microscale cellular problems are subjected to equivalent macroscale loads

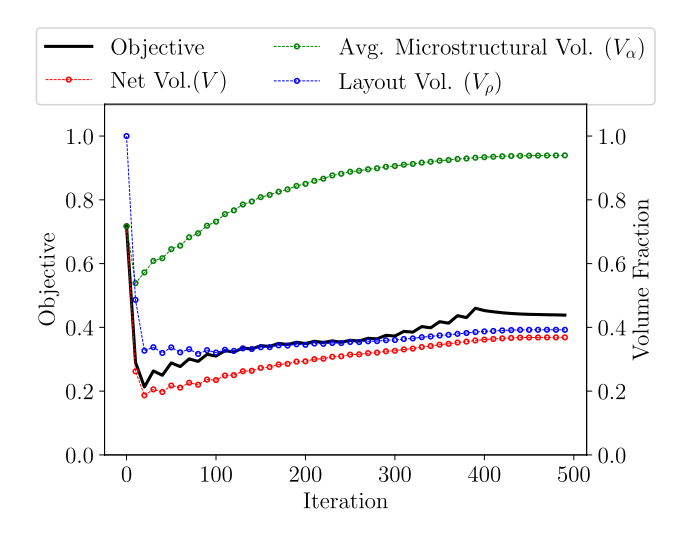
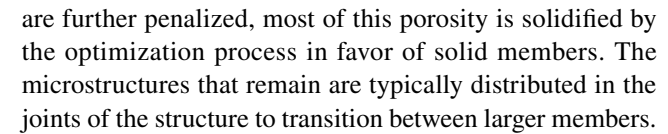


Fig. 18 The convergence of the optimized multiscale L-bracket design with elliptical microarchitecture—starting with an initial microstructural volume of $V_{\alpha}=0.7$ —is shown

designs, some infill porosity is preserved during the optimization. This is not the case with other objectives. In compliance minimization, for example, it is expected that the infill volume fraction approaches 100% (Sigmund et al 2016; Sigmund 2022). The preservation of some infill porosity illustrates the competition between the volume minimization and the satisfaction of the stress constraints. Early in the optimization before the hyperparameters of Table 3 have matured, the optimization favors the efficiency of a porous design with low infill volume fraction. As the stress constraint violations



5.1 Comparison of microstructure designs

The optimized designs for each of the three microstructures are shown in Fig. 20. The HS-truss design proved inappropriate for this framework and serves to aid our evaluation of this approach. Although the HS-truss is simply parameterized by one parameter (its effective density), the optimized failed to converge to a viable structure for the target stress limit of $\sigma_Y = 75$. For an increased stress limit of $\sigma_Y = 150$ and an increased characteristic length ratio of l/L = 1/40 = 0.0250, the HS-truss design converged to a suboptimal design with net volume fraction of 30%. The poor performance is attributed to the stress concentrations caused by the member connections in each truss. Although this design is stiffer than the ellipse microstructure at a given effective density, the HS-truss's proclivity to stress concentrations are an impediment to the optimization's progress.

The biotruss design alleviates stress concentrations through its smooth interfaces. Furthermore, the biotruss creates a much larger design space (10 parameters per microstructure). The optimized L-bracket design for the biotruss microarchitecture shown in Fig. 20 achieved a net volume fraction of 46%. Here we note that the parameterization for the biotruss results in a lower bulk modulus than the ellipse microstructure, as optimization of the bulk modulus via microscale optimization traditionally distributes material to the outside of each microstructure (Sigmund et al 2016). The biotruss is generally less stiff, so more material is required to satisfy the same stress constraints as the ellipse.

5.2 Comparison of different boundary conditions

Two new domains are defined in Figs. 21 and 22. The double L-bracket of Fig. 21 uses mixed loading and two reentrant corners to test the optimization framework. The double L-bracket domain is discretized into 5,632 microstructures with a characteristic length ratio of l/L = 1/80 = 0.0125. The stress concentration problem illustrated in Fig. 22 is derived from da Silva et al (2021a) and is discretized into 5000 microstructures with a characteristic length ratio of l/L = 1/100 = 0.01. The multiscale design optimization results are compared to the monoscale density-based topology optimization results in Table 4. Figures 23, 24, and 25 compare the optimized designs for density-based topology optimization and our multiscale approach with the elliptical microstructure.

The density-based formulation for stress-constrained design does not include any amplification caused by



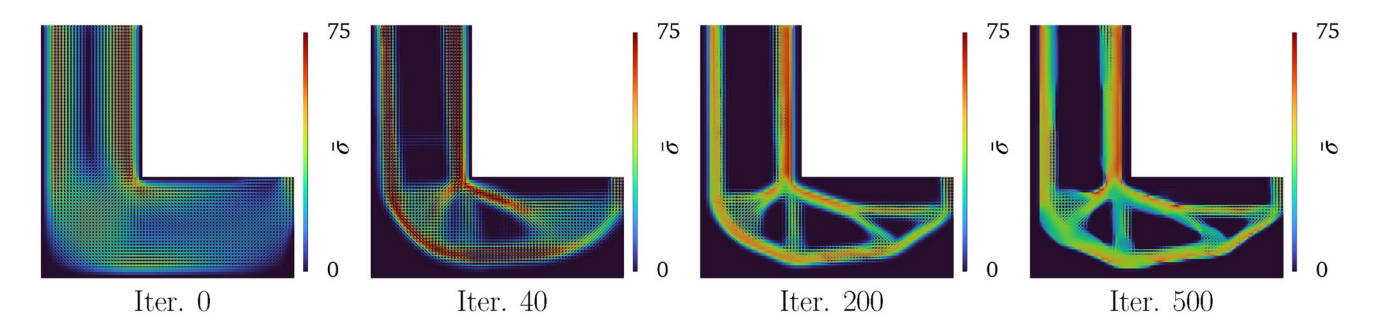


Fig. 19 The von Mises stress $\bar{\sigma}$ evaluated on an equivalent fullscale mesh is shown for the design problem outlined in Fig. 18

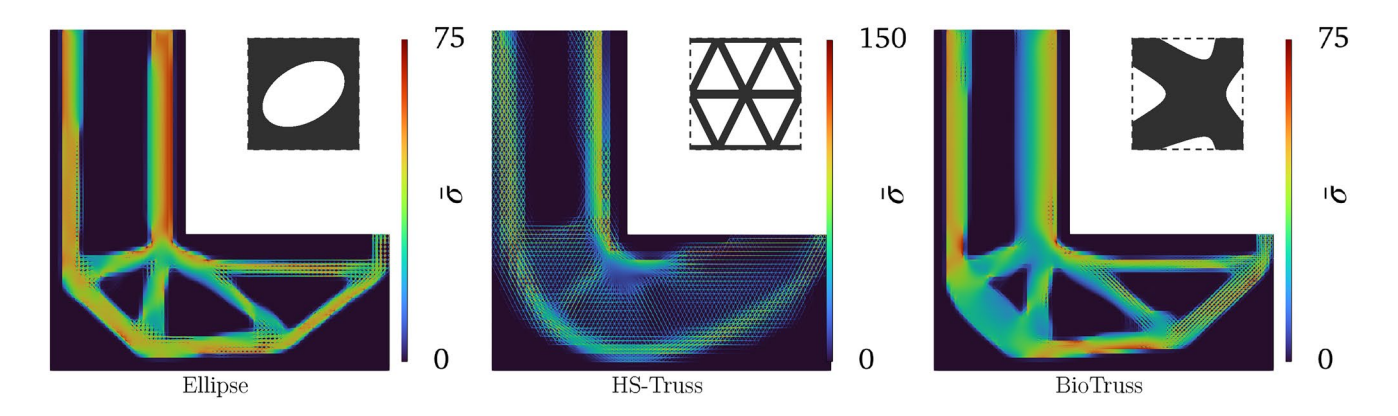
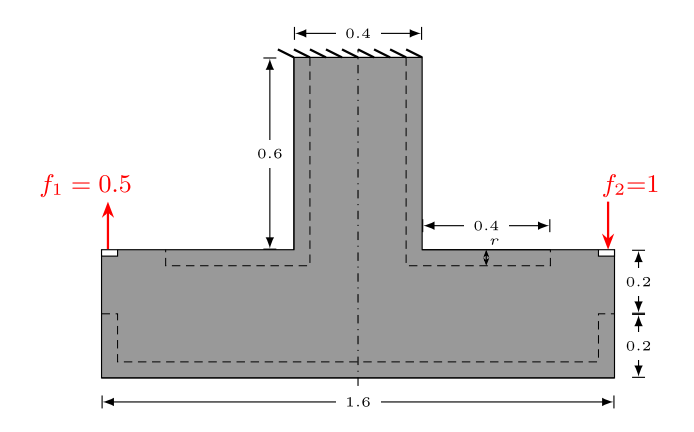


Fig. 20 The optimized results for three different microstructure designs are presented for the L-bracket benchmark problem



 $\begin{tabular}{ll} Fig. 21 The double L-bracket benchmark boundary conditions are shown including the buffer zone indicated by dashed lines \\ \end{tabular}$

intermediate microstructure designs, so $f_a=1$ for all values of the design variable ρ . Therefore, the pre-convergence designs offer a relaxed evaluation of stress. The density-based optimized designs subsequently feature smaller macroscale members compared to the multiscale designs. Although the multiscale designs attempt to compensate for this increased mass with some infill porosity, they fail to outperform the density-based formulations. Both formulations

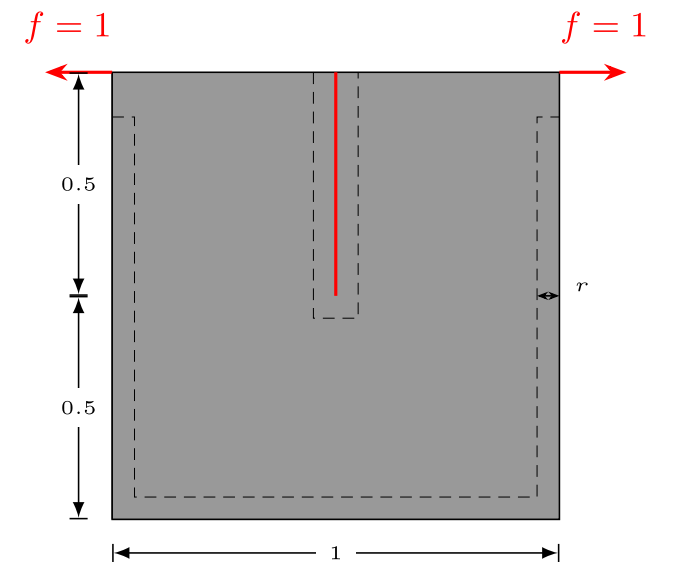


Fig. 22 The stress-concentration benchmark boundary conditions are shown including the buffer zone indicated by dashed lines

largely obey the prescribed stress constraints with all design examples resulting in a Y_F of 1–2%. The stress measured in the multiscale formulation is microstructure-aware, so



Table 4 Key characteristics of comparable optimized designs are presented

Example	Microstructure	V	$V_{ ho}$	V_{α}	Y_F
L-bracket					
	Density-based	0.261	_	_	0.017
	Ellipse $(V_a^0 = 1.0)$	0.333	0.347	0.958	0.014
	Ellipse $(V_{\alpha}^{0} = 0.7)$	0.369	0.392	0.939	0.013
	BioTruss	0.431	0.443	0.972	0.006
Double L-bracket					
	Density-based	0.271	_	_	0.018
	Ellipse	0.423	0.448	0.944	0.011
Stress Concentra-					
tion	Density-based	0.153	-	-	0.010
	Ellipse	0.212	0.238	0.892	0.014

the stress distribution in the multiscale designs is generally lower than the prescribed stress limit. Meanwhile, the density-based designs feature a larger portion of the structure near the stress limit.

Density-based

Fig. 23 The density-based topology optimized result is compared to the multiscale (ellipse microarchitecture) optimized result for the L-bracket benchmark problem

Density-based Multiscale 75 75 75

Multiscale

75

Fig. 24 The density-based topology optimized result is compared to the multiscale (ellipse microarchitecture) optimized result for the double L-bracket benchmark problem

5.3 Multifunctional design

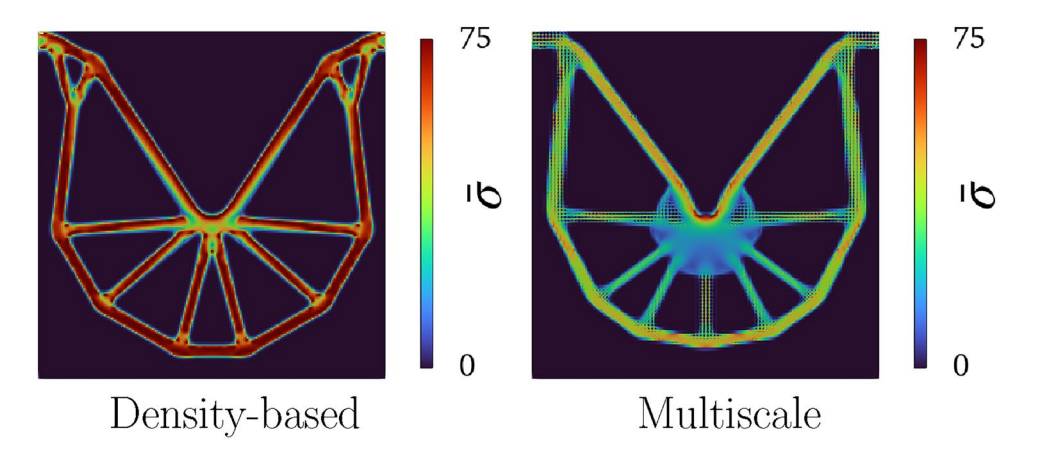
The previous section showed that the homogenization-based multiscale design optimization cannot outperform density-based topology optimization in pure volume minimization problems subjected to stress constraints (and indeed this trend continues with other objectives such as single-load structural compliance (Sigmund 2022)). These examples were included as a controlled metric for evaluating the presented multiscale framework for optimization with microstructural stress constraints. This framework is extensible to other objectives, as we will demonstrate in this section with a simple multifunctional design problem.

The multifunctional problem, described in Fig. 26, adds to the objective (42) a target displacement term to design a structure that (1) supports an external load and (2) maintains dimensional stability in a specific region:

$$\hat{\Theta} = \Theta + \frac{1}{N} \gamma \circ (\mathbf{u} - \mathbf{u}_T)^T (\mathbf{u} - \mathbf{u}_T)$$
(49)

75

Fig. 25 The density-based topology optimized result is compared to the multiscale (ellipse microarchitecture) optimized result for the stress-concentration benchmark problem



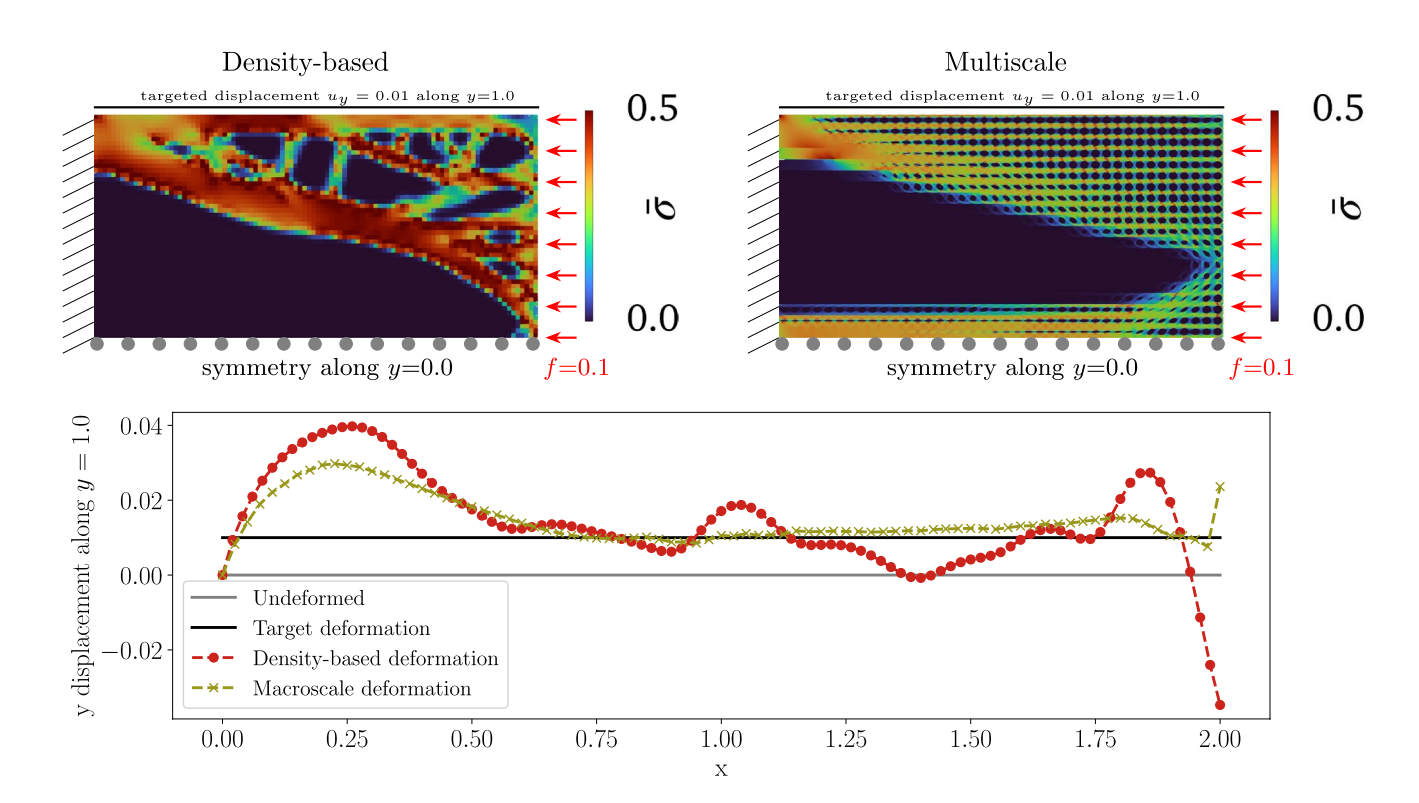


Fig. 26 The results of a stress-constrained design optimization problem in which a prescribed deformation is applied to one surface are compared. A beam is fixed on one end and subjected to a uniform load on its free end with a symmetry condition enforced about the

x axis. A target displacement is defined on the surface y = 1.0. The optimized designs are shown here along with the displacement of the final designs along the free surface

where u and u_T are the structure's displacement and its predefined target displacement respectively, γ is a vector of ones and zeros of size u with 1 indicating a targeted degree of freedom and 0 elsewhere, and N is a scalar normalization term for the number of targeted degrees of freedom. Multiscale approaches have been shown to perform well when considering this objective, as their expanded microstructural material property space allows for anisotropy that is not possible with density-based design (Wang et al 2020; Black and Najafi 2023). Sensitivity analysis of this objective is performed in Black and Najafi (2023).

The resulting formulation represents a volume minimization problem subjected to stress constraints ($\sigma_Y = 0.5$) and a prescribed deformation. The example in Fig. 26 shows a target displacement of 0.01 in the y direction on one surface of a beam subjected to compressive loading f = 0.1 and symmetry boundary conditions. In this example, a 2 × 1 domain is discretized into 100 × 50 elements for



density-based optimization or 40×20 microstructures for multiscale optimization. After 500 iterations following the parameter update schedule defined in Table 3, the density-based design converged to a final volume fraction of 33%, and the multiscale design converged to a final volume fraction of 43%. Interestingly, although the multiscale design required more material, the anisotropy of the microstructural material model converged to a better targeted displacement; the L_2 norm of $(u-u_T)$ was 0.133 for the density-based design and 0.070 for the multiscale design. Figure 26 also shows that the peak deviation from the target displacement is also reduced in the multiscale formulation.

6 Conclusion

This work presented a methodology for stress-constrained multiscale design optimization of hierarchical structures. The multiscale design space considered the macroscale layout of the structure and the microscale parameterization of local geometry, producing a hierarchical system of connected microstructures. To approximate the local stress in each microstructure without modeling the expensive fullscale model, two successive homogenization steps were performed. First, the macroscale response was approximated based on the homogenized, first-order material properties of each microstructure. Next, using second-order homogenization, the local stress was evaluated in each microstructure. The combination of these homogenization methods proved an effective approximation of the stress amplification factor induced by local microarchitecture with poor scale separation. The optimization approach implemented neural network surrogate models for each of the homogenization steps. The first class of neural network approximated the effective properties of each microstructure based on its geometric parameterization, and the second class of neural network estimated the stress amplification factor as a function of the microstructure's geometric parameterization and its deformed configuration. With an augmented lagrangian formulation of stress constraints, a series of example problems were presented that minimized the volume of a multiscale structure subjected to stress constraints.

The examples illustrate several important attributes of the presented methodology. We note that the system of neural network surrogates were sufficiently accurate in ensuring stress constraints were accurately modeled during the optimization process. The optimization performance is also dependent on the choice of microstructure parameterization. This parameterization, which was restricted to perfect cellto-cell connections that respect the assumption of periodicity, must produce a sufficiently stiff microstructure without inducing stress concentrations. Furthermore, the number of design parameters should be carefully considered, as each new parameter requires an additional solve of the sensitivity's adjoint variable. The data generation time for the training datasets required to train both classes of neural network should also be considered, as more complicated designs may require more data to capture the entire design space.

The multiscale approach presented in this work does not outperform density-based (monoscale) approaches in the minimization of structural volume subjected to stress constraints. In this particular objective, the augmented lagrangian approach was able to enforce stress constraints with minimal violations (*cf.* Table 4). The freedom of density-based design in controlling the structural layout proved more beneficial in the provided examples, producing a lower overall structural volume. It is our view then that the application of multiscale is more appropriate for multiobjective or multiphysics problems such as optimizing buckling resistance or diffusivity. In these scenarios, the method presented here would be an effective approach to including microstructural stress-constraints in the optimization formulation.

Consequently, the main contribution of this work lies in the multiscale design formulation. Incorporating secondorder homogenization techniques, this formulation included local information related to the microstructure's stress. The neural network surrogate model served to include this local information in the optimization formulation. We have demonstrated the viability of this approach in structural optimization; the surrogate model was able to successfully navigate the multiscale design space and enforce local stress constraints to the same tolerance as density-based topology optimization Table 4. For different objectives (e.g., design for maximum energy absorption, design for maximum buckling load) and especially for models with local material nonlinearity, the inclusion of microstructure-level mechanics is critical to successful design optimization. The framework presented here will be critical to extending multiscale design in these areas.

The second-order evaluation of microstructure response enabled the realization of microstructures at the observable scale. We considered an infinitesimal strain formulation of uncoupled second-order homogenization. Here, the first-order macroscale response was evaluated, then the element shape functions were used to approximate second-order strains in the microscale. We showed that the uncoupled model produced accurate analysis when the separation of scales decreased. Future work should evaluate a second-order scheme that incorporates higher-order stresses in the macroscale.

The design framework presented in this work is readily extensible to new microstructures and 3D designs. The computational cost of extension to 3D should not be underestimated, as both the computational cost macroscale analysis and microstructural analyses will increase dramatically. As with density-based (monoscale) design techniques, this



multiscale technique evaluated stresses based on a nonconforming mesh, relying on filtering and interpolation of stresses to characterize the design. Future work may improve this evaluation with isogeometric finite element methods.

This work has built an optimization approach that enriches the information exchange between the local material scale and the greater structure. Additionally, the second-order approach to local analysis is a promising method to relieve the computational burdens associated with the separation of scales. Finally, the machine learning approach used here remains favorable because of its low data generation costs, quick and efficient training, and significant contribution to the design model.

Acknowledgements The authors would like to acknowledge support from Drexel University. N. Black is thankful for support from the GAANN Grant [No. P200A190036]. The work is also supported by the NSF CAREER Award CMMI-2143422.

Declarations

Conflict of interest The authors declare that they have no Conflict of interest.

Replication of results Comprehensive implementation details were provided and the authors are confident that the work if reproducible. For further details and access to the training datasets used in this work, readers are encouraged to contact the authors.

Open Access This article is licensed under a Creative Commons Attribution 4.0 International License, which permits use, sharing, adaptation, distribution and reproduction in any medium or format, as long as you give appropriate credit to the original author(s) and the source, provide a link to the Creative Commons licence, and indicate if changes were made. The images or other third party material in this article are included in the article's Creative Commons licence, unless indicated otherwise in a credit line to the material. If material is not included in the article's Creative Commons licence and your intended use is not permitted by statutory regulation or exceeds the permitted use, you will need to obtain permission directly from the copyright holder. To view a copy of this licence, visit http://creativecommons.org/licenses/by/4.0/.

References

- Alacoque L, Watkins RT, Tamijani AY (2021) Stress-based and robust topology optimization for thermoelastic multi-material periodic microstructures. Comput Methods Appl Mech Eng 379:113749. https://doi.org/10.1016/j.cma.2021.113749
- Alberdi R, Dingreville R, Robbins J et al (2020) Multi-morphology lattices lead to improved plastic energy absorption. Mater Des 194:108883. https://doi.org/10.1016/j.matdes.2020.108883
- Allaire G (2002) Shape optimization by the homogenization method. Springer, New York
- Allaire G (2012) A brief introduction to homogenization and miscellaneous applications. ESAIM Proc 37:1–4. https://doi.org/10.1051/ proc/201237001
- Allaire G, Jouve F, Maillot H (2004) Topology optimization for minimum stress design with the homogenization method.

- Struct Multidisc Optim 28(2):87-9. https://doi.org/10.1007/s00158-004-0442-8
- Bendsøe MP, Kikuchi N (1988) Generating optimal topologies in structural design using a homogenization method. Comput Methods Appl Mech Eng 71(2):197–22. https://doi.org/10.1016/0045-7825(88)90086-2
- Black N, Najafi AR (2023) Deep neural networks for parameterized homogenization in concurrent multiscale structural optimization. Struct Multidisc Optim 66(1):1–2. https://doi.org/10.1007/s00158-022-03471-y
- Blanco PJ, Sánchez PJ, de Souza Neto EA et al (2016) The method of multiscale virtual power for the derivation of a second order mechanical model. Mech Mater 99:53–67. https://doi.org/10.1016/j.mechmat.2016.05.003
- Blanco PJ, Sánchez PJ, de Souza Neto EA et al (2016) Variational Foundations and Generalized Unified Theory of RVE-Based Multiscale Models. Arch Comput Methods Eng 23(2):191–253. https://doi.org/10.1007/s11831-014-9137-5
- Bruns TE, Tortorelli DA (2001) Topology optimization of non-linear elastic structures and compliant mechanisms. Comput Methods Appl Mech Eng 190(26):3443–345. https://doi.org/10.1016/S0045-7825(00)00278-4
- Cheng GD, Guo X (1997) ϵ -relaxed approach in structural topology optimization. Struct Optim 13(4):258–266. https://doi.org/10.1007/BF01197454
- Cheng L, Bai J, To AC (2019) Functionally graded lattice structure topology optimization for the design of additive manufactured components with stress constraints. Comput Methods Appl Mech Eng 344:334–35. https://doi.org/10.1016/j.cma.2018.10.010 (https://www.sciencedirect.com/science/article/pii/S004578251 8305061)
- Coelho PG, Guedes JM, Cardoso JB (2019) Topology optimization of cellular materials with periodic microstructure under stress constraints. Struct Multidisc Optim 59(2):633–64. https://doi.org/10.1007/s00158-018-2089-x
- Coelho PG, Barroca BC, Conde FM et al (2021) Minimization of maximal von Mises stress in porous composite microstructures using shape and topology optimization. Struct Multidisc Optim 64(4):1781–1799. https://doi.org/10.1007/s00158-021-02942-y
- Collet M, Noël L, Bruggi M et al (2018) Topology optimization for microstructural design under stress constraints. Struct Multidisc Optim 58(6):2677–2679. https://doi.org/10.1007/s00158-018-2045-9
- Conde FM, Coelho PG, Guedes JM (2022) Multi-material and strengthoriented microstructural topology optimization applied to discrete phase and functionally graded materials. Struct Multidisc Optim 65(4):1–22. https://doi.org/10.1007/s00158-022-03209-w
- da Silva GA, Aage N, Beck AT et al (2021) Local versus global stress constraint strategies in topology optimization: a comparative study. Int J Numer Methods Eng 122(21):6003–603. https://doi.org/10.1002/nme.6781
- da Silva GA, Aage N, Beck AT et al (2021) Three-dimensional manufacturing tolerant topology optimization with hundreds of millions of local stress constraints. Int J Numer Methods Eng 122(2):548–578. https://doi.org/10.1002/nme.6548
- De Souza Neto EA, Blanco PJ, Sánchez PJ et al (2015) An RVE-based multiscale theory of solids with micro-scale inertia and body force effects. Elsevi. https://doi.org/10.1016/j.mechmat.2014.10.007
- Djourachkovitch T, Blal N, Hamila N et al (2021) Multiscale topology optimization of 3D structures: a micro-architectured materials database assisted strategy. Comput Struct 255:106574. https://doi.org/10.1016/j.compstruc.2021.106574
- Duysinx P, Bendsøe MP (1998) Topology optimization of continuum structures with local stress constraints. Int J Numer Methods Eng 43(8):1453–1478. https://doi.org/10.1002/(SICI)1097-0207(19981230)43:8<1453::AID-NME480>3.0.CO;2-2



- Duysinx P, Sigmund O (1998). New developments in handling stress constraints in optimal material distributio. https://doi.org/10.2514/6.1998-4906
- Ferrer A, Geoffroy-Donders P, Allaire G (2021) Stress minimization for lattice structures. Part I: Micro-structure design. Philos Trans R Soc A 379(2201):2020010. https://doi.org/10.1098/rsta.2020.0109
- Groen JP, Sigmund O (2017) Homogenization-based topology optimization for high-resolution manufacturable microstructures. Int J Numer Meth Eng 113(8):1148–116. https://doi.org/10.1002/nme. 5575
- Groen JP, Thomsen CR, Sigmund O (2021) Multi-scale topology optimization for stiffness and de-homogenization using implicit geometry modeling. Struct Multidisc Optim 63(6):2919–2934. https://doi.org/10.1007/s00158-021-02874-7
- Guedes J, Kikuchi N (1990) Preprocessing and postprocessing for materials based on the homogenization method with adaptive finite element methods. Comput Methods Appl Mech Eng 83(2):143–198. https://doi.org/10.1016/0045-7825(90)90148-F
- Hassani B, Hinton E (1998) A review of homogenization and topology optimization I-homogenization theory for media with periodic structure. Comput Struct 69(6):707–717. https://doi.org/10.1016/S0045-7949(98)00131-X
- Ho-Nguyen-Tan T, Kim HG (2023) Stress-constrained concurrent two-scale topology optimization of functionally graded cellular structures using level set-based trimmed quadrilateral meshes. Struct Multidisc Optim 66(6):1–2. https://doi.org/10.1007/s00158-023-03572-2
- Ito K, Kunisch K (1990) The augmented Lagrangian method for equality and inequality constraints in Hilbert spaces. Math Program 46(1):341–360. https://doi.org/10.1007/BF01585750
- Kingma DP, Ba J (2017) Adam: a method for stochastic optimization.https://doi.org/10.48550/arXiv.1412.6980
- Kochmann DM, Bertoldi K (2017) exploiting microstructural instabilities in solids and structures: from metamaterials to structural transitions. Appl Mech Rev 69:5. https://doi.org/10.1115/1.4037966
- Kouznetsova V, Geers MGD, Brekelmans WAM (2002) Multi-scale constitutive modelling of heterogeneous materials with a gradient-enhanced computational homogenization scheme. Int J Numer Methods Eng 54(8):1235–1260. https://doi.org/10.1002/ nme.541
- Kouznetsova VG, Geers MGD, Brekelmans WAM (2004) Multi-scale second-order computational homogenization of multi-phase materials: a nested finite element solution strategy. Comput Methods Appl Mech Eng 193(48):5525–5550. https://doi.org/10.1016/j. cma.2003.12.073
- Le C, Norato J, Bruns T et al (2010) Stress-based topology optimization for continua. Struct Multidisc Optim 41(4):605–620. https://doi.org/10.1007/s00158-009-0440-y
- Lian H, Christiansen AN, Tortorelli DA et al (2017) Combined shape and topology optimization for minimization of maximal von Mises stress. Struct Multidisc Optim 55(5):1541–1555. https://doi.org/10.1007/s00158-017-1656-x
- Luo Y, Wang MY, Kang Z (2013) An enhanced aggregation method for topology optimization with local stress constraints. Comput Methods Appl Mech Eng 254:31–4. https://doi.org/10.1016/j.cma. 2012.10.019
- Miehe C, Koch A (2002) Computational micro-to-macro transitions of discretized microstructures undergoing small strains. Arch Appl Mech 72(4):300–31. https://doi.org/10.1007/s00419-002-0212-2
- Najafi AR, Safdari M, Tortorelli DA et al (2021) Multiscale design of nonlinear materials using a Eulerian shape optimization scheme. Int J Numer Meth Eng 122(12):2981–301. https://doi.org/10.1002/ nme.6650
- Nakshatrala PB, Tortorelli DA, Nakshatrala KB (2013) Nonlinear structural design using multiscale topology optimization. Part

- I: Static formulation. Comput Methods Appl Mech Eng 261–262:167–176. https://doi.org/10.1016/j.cma.2012.12.018
- Nguyen VD, Becker G, Noels L (2013) Multiscale computational homogenization methods with a gradient enhanced scheme based on the discontinuous Galerkin formulation. Comput Methods Appl Mech Eng 260:63–77. https://doi.org/10.1016/j.cma.2013.03.024
- Pantz O, Trabelsi K (2008) A post-treatment of the homogenization method for shape optimization. SIAM J Control Optim 47(3):1380–139. https://doi.org/10.1137/070688900
- Pereira JT, Fancello EA, Barcellos CS (2004) Topology optimization of continuum structures with material failure constraints. Struct Multidisc Optim 26(1):50–6. https://doi.org/10.1007/s00158-003-0301-z
- Picelli R, Townsend S, Kim HA (2020) Microstructural stress shape optimization using the level set method. J Mech Des 142:11. https://doi.org/10.1115/1.4047152
- Rodrigues Lopes IA, Andrade Pires FM (2022) Unlocking the potential of second-order computational homogenisation: an overview of distinct formulations and a guide for their implementation. Arch Comput Methods Eng 29(3):1339. https://doi.org/10.1007/s11831-021-09611-9
- Rozvany GIN, Zhou M, Birker T (1992) Generalized shape optimization without homogenization. Struct Optim 4(3):250–252. https://doi.org/10.1007/BF01742754
- Senhora FV, Giraldo-Londoño O, Menezes IFM et al (2020) Topology optimization with local stress constraints: a stress aggregation-free approach. Struct Multidisc Optim 62(4):1639–1668. https://doi.org/10.1007/s00158-020-02573-9
- Sigmund O (2022) On benchmarking and good scientific practise in topology optimization. Struct Multidisc Optim 65(11):1–10. https://doi.org/10.1007/s00158-022-03427-2
- Sigmund O, Aage N, Andreassen E (2016) On the (non-)optimality of Michell structures. Struct Multidisc Optim 54(2):361–373. https://doi.org/10.1007/s00158-016-1420-7
- Surjadi JU, Gao L, Du H et al (2019) Mechanical metamaterials and their engineering applications. Adv Eng Mater 21(3):1800864. https://doi.org/10.1002/adem.201800864
- Svanberg K (1987) The method of moving asymptotes-a new method for structural optimization. Int J Numer Meth Eng 24(2):359–37. https://doi.org/10.1002/nme.1620240207
- Träff E, Sigmund O, Groen J (2018) Simple single-scale microstructures based on optimal rank-3 laminates. arXiv https://doi.org/10.48550/arXiv.1809.03942
- Wallin M, Tortorelli DA (2020) Nonlinear homogenization for topology optimization. Mech Mater 145:10332. https://doi.org/10.1016/j.mechmat.2020.103324
- Wang C, Zhu JH, Zhang WH et al (2018) Concurrent topology optimization design of structures and non-uniform parameterized lattice microstructures. Struct Multidisc Optim 58(1):35–50. https://doi.org/10.1007/s00158-018-2009-0
- Wang F, Sigmund O (2020) Numerical investigation of stiffness and buckling response of simple and optimized infill structures. Struct Multidisc Optim 61(6):2629–2630. https://doi.org/10.1007/s00158-020-02525-3
- Wang F, Lazarov BS, Sigmund O (2011) On projection methods, convergence and robust formulations in topology optimization. Struct Multidisc Optim 43(6):767–78. https://doi.org/10.1007/ s00158-010-0602-y
- Wang L, Chan YC, Ahmed F et al (2020) Deep generative modeling for mechanistic-based learning and design of metamaterial systems. Comput Methods Appl Mech Eng 372:113377. https:// doi.org/10.1016/j.cma.2020.113377 (https://www.sciencedirect. com/science/article/pii/S0045782520305624)
- Wegst UGK, Bai H, Saiz E et al (2015) Bioinspired structural materials. Nat Mater 14:23–3. https://doi.org/10.1038/nmat4089



- White DA, Arrighi WJ, Kudo J et al (2018) Multiscale topology optimization using neural network surrogate models. Comput Methods Appl Mech Eng 346:1118–113. https://doi.org/10.1016/j.cma.2018.09.007 (https://linkinghub.elsevier.com/retrieve/pii/S004578251830450X)
- Wu J, Sigmund O, Groen JP (2021) Topology optimization of multiscale structures: a review. Struct Multidisc Optim 63(3):1455– 1458. https://doi.org/10.1007/s00158-021-02881-8
- Wu J, Wang W, Gao X (2021) Design and optimization of conforming lattice structures. IEEE Trans Visual Comput Graph 27(1):43–5. https://doi.org/10.1109/TVCG.2019.2938946
- Xia L, Breitkopf P (2014) Concurrent topology optimization design of material and structure within FE2 nonlinear multiscale analysis framework. Comput Methods Appl Mech Eng 278:524–54. https://doi.org/10.1016/j.cma.2014.05.022
- Zhang JZ, Sharpe C, Seepersad CC (2020) Stress-constrained design of functionally graded lattice structures with spline-based dimensionality reduction. J Mech Des 142:9. https://doi.org/10.1115/1. 4046237
- Zhang ZJ, Butscher A, Watts S et al (2022) Anisotropic yield models for lattice unit cell structures exploiting orthotropic symmetry. Comput Methods Appl Mech Eng 394:11493. https://doi.org/10.1016/j.cma.2022.114935

- Zhao L, Xu B, Han Y et al (2021) Concurrent design of composite macrostructure and cellular microstructure with respect to dynamic stress response under random excitations. Compos Struct 257:113123. https://doi.org/10.1016/j.compstruct.2020.113123
- Zhao R, Zhao J, Wang C (2021) Stress-constrained concurrent topology optimization of two-scale hierarchical structures. Int J Numer Methods Eng 122(21):6126–615. https://doi.org/10.1002/nme. 6785
- Zhao R, Zhao J, Wang C (2022) Stress-constrained multiscale topology optimization with connectable graded microstructures using the worst-case analysis. Int J Numer Methods Eng 123(8):1882–190. https://doi.org/10.1002/nme.6920
- Zhou M, Rozvany GIN (1991) The COC algorithm, Part II: Topological, geometrical and generalized shape optimization. Comput Methods Appl Mech Eng 89(1):309–33. https://doi.org/10.1016/0045-7825(91)90046-9

Publisher's Note Springer Nature remains neutral with regard to jurisdictional claims in published maps and institutional affiliations.

